International Journal of Biological Macromolecules 279 (2024) 135089

Contents lists available at ScienceDirect

International Journal of Biological Macromolecules

journal homepage: www.elsevier.com/locate/ijbiomac

Differential pathogenetic mechanisms of mutations in helix 2 and helix 6 of rhodopsin

Andrea Bighinati [a,1], Sara D'Alessandro [a,1], Angelo Felline [a], Christina Zeitz [b], Béatrice Bocquet [c], Livio Casarini [d], Vasiliki Kalatzis [e], Isabelle Meunier [c], Francesca Fanelli [a,*], Gaël Manes [e,*,1], Valeria Marigo [a,*,1]

[a] University of Modena and Reggio Emilia, Department of Life Sciences, via G. Campi 287, 41125 Modena, Italy
[b] Sorbonne Université, INSERM, CNRS, Institut de la Vision, 17 rue Moreau, 75012 Paris, France
[c] INM, Univ Montpellier, INSERM, CHU Montpellier, 80 Av. Augustin Fliche, 34295 Montpellier, France
[d] University of Modena and Reggio Emilia, Unit of Endocrinology, Department of Biomedical, Metabolic and Neural Sciences, via P. Giardini, 1355, 41126 Baggiovara, Modena, Italy
[e] INM, Univ Montpellier, INSERM, 80 rue Augustin Fliche, 34091 Montpellier, France

ARTICLE INFO

Keywords:
GPCR
Molecular simulations
BRET
mini G protein
Visual arrestin
CSNB

ABSTRACT

Variants in rhodopsin (RHO) have been linked to autosomal dominant congenital stationary night blindness (adCSNB), which affects the ability to see in dim light, and the pathogenetic mechanism is still not well understood. In this study we report two novel RHO variants found in adCSNB families, p.W265R and p.A269V, that map in the sixth transmembrane domain of RHO protein. We applied *in silico* molecular simulation and *in vitro* biochemical and molecular studies to characterize the two new variants and compare the molecular determinants to two previously characterized adCSNB variants, p.G90D and p.T94I, that map in the second transmembrane domain of the RHO protein. We demonstrate that W265R and A269V cause constitutive activation of RHO with light-independent G protein coupling and impaired binding to arrestin. Differently, G90D and T94I are characterized by slow kinetics of RHO activation and deactivation. This study provides new evidence on the differential contribution of transmembrane α-helixes two and six to the interaction with intracellular transducers of RHO and mutations in these helixes result in a similar phenotype in patients but with distinct molecular effects.

1. Introduction

Autosomal dominant congenital stationary night blindness (adCSNB; MIM #163500) has been linked to pathogenic variants in three genes: *GNAT1* encoding the rod transducin G protein alpha subunit (Gt), phosphodiesterase 6 beta (*PDE6B*) and rhodopsin (*RHO*) [1]. Pathogenic variants in RHO, the rod-specific G protein-coupled receptor (GPCR), can cause adCSNB [2] or autosomal dominant retinitis pigmentosa (adRP) [3] and, more rarely, autosomal recessive RP [4,5]. RHO is the visual pigment of rod photoreceptor cells composed of an apoprotein, called opsin, linked at the level of lysine 296 (K296) *via* a Schiff base to the chromophore 11-*cis*-retinal, and its function is to activate the phototransduction cascade following light capture [6]. Upon photon absorption and *cis-trans* isomerization of 11-*cis*-retinal, RHO transits to the signaling active metarhodopsin II (MII) states that trigger the visual phototransduction cascade by coupling to Gt [7]. The signal is terminated upon phosphorylation by the G-protein coupled receptor kinase 1 (GRK1) and by binding to visual arrestin (ARR1), encoded by the *SAG* gene.

Over 200 different variants in *RHO*, listed in the human genome mutation database (HGMD), are linked to adRP, but only five pathogenic variants have been found in adCSNB patients so far (Table 1) [8–11]. The majority of adRP RHO variants cause protein misfolding and retention into the endoplasmic reticulum (ER) [12]. Within the large group of RHO variants, a minority affects the functionality of the protein by altering either the correct delivery to the disc membrane, its phosphorylation, or its coupling to intracellular proteins (*e.g.* Gt or ARR1) [13]. The five adCSNB variants discovered so far cause a milder phenotype compared to RP variants, because they affect vision in dim light and the phenotype does not progress to retinal degeneration. While

* Corresponding authors.
E-mail addresses: francesca.fanelli@unimore.it (F. Fanelli), gael.manes@inserm.fr (G. Manes), valeria.marigo@unimore.it (V. Marigo).
[1] These authors equally contributed to this study.

https://doi.org/10.1016/j.ijbiomac.2024.135089
Received 24 July 2024; Received in revised form 20 August 2024; Accepted 24 August 2024
Available online 26 August 2024

the adRP variants are distributed in the entire protein, the five adCSNB variants locate in the retinal-binding-site portions of three alpha-helixes (H), *i.e.* H2 (G90D and T94I), H3 (E113K), and H7 (A292E and A295V). All but one of them consist in non-conservative replacements, *i.e.* neutral-to-anionic (G90D and A292E), anionic-to-cationic (E113K), and polar-to-hydrophobic (T94I) amino-acid changes. Most of adCSNB-associated variants have been shown to constitutively activate Gt *in vitro* [9,11,14–16]. In the mouse model bearing the G90D mutation, rod photoreceptors exhibit a diminished light sensitivity, which is comparable to wild type (WT) rods illuminated with steady light [17]. The two G90D and T94I variants have been characterized at the atomic detail (PDB codes 4bez active state opsin apoprotein and 5dys MII state, respectively). In the case of G90D, the replacing aspartate displaces E113, the 11-*cis*-retinal counterion in the dark state, and forms a salt bridge with K296, thus possibly stabilizing an active opsin conformation [18]. The replacing isoleucine in T94I establishes a direct van der Waals interaction with K296, thus contributing to the prolongation of the MII signaling active state of RHO [19]. A common feature of G90D and T94I would be the ability of both replacing amino acids to interact with K296, thus altering the dark state by weakening the interaction between the Schiff base and its counterion E113 [18,19].

The mechanism by which the adCSNB variants are pathogenic is still not well understood. While G90D and T94I variants could be phosphorylated *in vitro* by GRK1, G90D, but not T94I, showed a reduced binding to ARR1 and lower binding to 11-*cis*-retinal [18,20]. T94I was reported to increase the half-time of the MII form with slower kinetics of retinal release [19]. A295V mutant was, otherwise, suggested to constitutively activate Gt [16].

Herein we report the identification of p.W265R and p.A269V (hereafter indicated as W265R and A269V) as novel adCSNB-linked RHO variants. These variants lie in the retinal binding-site portion of H6. Insights into the pathogenetic effects of the variants were acquired by combining molecular dynamics (MD) and docking simulations, *in vitro* subcellular localization and protein-protein proximity assays based on Bioluminescence Resonance Energy Transfer (BRET) to evaluate interactions with G-protein and ARR1. The two new adCSNB variants (H6-variants) were compared to the previously characterized G90D and T94I variants (H2-variants). Interestingly, the two novel H6-variants, while not causing structural misfolding, displayed constitutive coupling to G-protein in the absence of retinal and light activation. H6-variants also showed no or reduced binding to ARR1. Overall, our data suggest that the novel adCSNB H6-variants diverge from the previously characterized H2-variants in kinetics and coupling with the G-protein and ARR1.

2. Methods

2.1. Clinical examination

The study was approved by the Montpellier University Hospital, France (ID IRB-MTP_2021_11_202100959). The investigators followed the tenets of the Declaration of Helsinki. Informed consent for clinical examination and genetic analysis was obtained from the patients, according to approved protocols of the Montpellier University Hospital.

Patients had standard ophthalmologic examination (refractometry, visual acuity, slit-lamp examination, applanation tonometry, and funduscopy). Full-field electroretinograms (ERGs) were recorded using a Ganzfeld apparatus (Metrovision) with a bipolar contact lens electrode on maximally dilated pupils according to the International Society for Clinical Electrophysiology of Vision (ISCEV) protocol [21]. For numerical values, visual acuity was measured with Snellen charts in decimal numbers. Goldmann visual field was quantified by counting the number of subdivisions of the Goldmann grid within the areas of the V4e isopter and expressed as a percentage of the normal visual field. Dark adaptometry was performed with a Goldman Weekers apparatus and the responses were recorded at 11° above fixation after 3 min of pigment bleaching.

2.2. Variant screening

Genomic DNA was extracted from leucocytes using the FlexiGen DNA kit (Qiagen). The DNA samples were quantified by spectrophotometry and diluted to 25 ng/μl for PCR amplification. Coding exons and adjacent intronic regions of *RHO* (NM_000539; primer pairs and PCR conditions are available on request) were sequenced with an Applied Biosystems 3130xL genetic analyzer using a BigDye Terminator cycle sequencing ready reaction kit V3.1 (Applied Biosystems) following manufacturer's instructions. Sequence analysis was performed using the Collection and Sequence Analysis software package (Applied Biosystems). SIFT (Sorting Intolerant From Tolerant), PolyPhen2 (Polymorphism Phenotyping 2), PROVEAN (Protein Variation Effect Analyzer), aGVGD (align Grantham Variation and Grantham Deviation), Varsome, REVEL (Rare Exome Variant Ensemble Learner) and CADD

Table 1
Summary of adCSNB *RHO* (NM_000539.3) pathogenic variants.

Nucleotide change	Protein change	Exon	Protein region	gnomAD	VarSome DANN	PPhen2	SIFT	PROVEAN	aGVGD	REVEL	CADD	Reference
c.269G>A	p.G90D	1	H2	0	LP 0.9987	PRO	DAM	DEL	C65	0.784 DAM	27.50	Rao et al., 1994
c.281C>T	p.T94I	1	H2	0	LP 0.9988	PRO	DAM	NEU	C65	0.665 DAM	24.50	al-Jandal et al., 1999
c.337G>A	p.E113K	1	H3	0	LP 0.9993	PRO	DAM	DEL	C55	0.578 DAM	27.30	Reiff et al., 2016
c.793T>C	p.W265R	4	H6	0	LP 0.9968	PRO	DAM	DEL	C65	0.949 DAM	31.00	Present study
c.806C>T	p.A269V	4	H6	0	LP 0.9992	PRO	DAM	DEL	C55	0.540 DAM	25.20	Present study
c.875C>A	p.A292E	4	H7	0	LP 0.992	POS	DAM	DEL	C65	0.571 DAM	23.45	Dryja et al., 1993
c.884C>T	p.A295V	4	H7	0	LP 0.9993	PRO	DAM	DEL	C55	0.628 DAM	25.00	Zeitz et al., 2008

gnomAD, Genome Aggregation Database.
VarSome: LP, likely pathogenic. DANN score ranges from 0 to 1, with 1 given to the variants predicted to be the most damaging.
PPhen2, PolyPhen2, POS for possibly damaging, PRO for probably damaging, BEN for benign.
SIFT, TOL for tolerated, DAM for damaging.
PROVEAN (Prediction with cutoff = −2.5), DEL for deleterious, NEU for neutral.
aGVGD, align-Grantham Variation with Grantham Deviation, from C0 (neutral) to C65 (the most likely pathogenic).
REVEL, Rare Exome Variant Ensemble Learner, scores range from 0 to 1, DAM for damaging, with 1 given to the variants predicted to be the most damaging.
CADD, Combined Annotation Dependent Depletion, above >30, highly pathogenic, above >20 pathogenic, between 15 and 20, likely pathogenic.

(Combined Annotation Dependent Depletion) were used to predict possible impacts of missense variants.

2.3. Computational experiments

Prediction of the Pearson Correlation Coefficient (PCC) accounting for ER retention of W265R and A269V adCSNB variants was based on a computational model that we previously described [22]. The methodology consisted in mechanical unfolding simulations (by Steered Molecular Dynamics (SMD)) of mutant RHO in a hexameric or nonameric homo-oligomer followed by protein structure network (PSN) analysis. SMD simulations were carried out by means of the CHARMM force field (in all-atom mode) [23], using the GBSW implicit membrane/water model [24].

The same force field and solvent model were employed for equilibrium MD simulations by using essentially the same computational setup that we previously described [12]. Such simulations were carried out on the H2- and H6-variants in their active opsin and MII states. For the G90D and T94I H2-variants (sequence 1–323), the crystal structures 4bez and 5dys were used as inputs for the opsin and MII states added or deprived of all-*trans*-retinal. For the W265R and A269V H6-variants, the active opsin and MII states used as input (sequence 1–323) were achieved by mutating the crystal structure of active opsin (PDB: 3cap [25]) and of MII (PDB: 3pxo [26]), respectively. To reduce the degrees of freedom, while letting helices move as rigid bodies, intrahelical distance restraints were applied to the backbone nitrogen and oxygen atoms involved in H-bonds. Moreover, to avoid excessive approaching of H3 and H7, distance restraints were set between the Cα-atom of R135 and both Y306 and N310. The native disulfide bridge between C110 and C187 was allowed to form; the artificial stabilizing disulfide bridge between C2 and C282 present in the crystal structures of the two H2-variants was kept in those variants. Finally, distance restraints were set between the oxygen atoms of a number of structural water molecules and the surrounding H-bonding partners. For all distance restraints, the scaling factor was set to 10 and the force constant at 300 K was set to 10 kcal/mol/Å. Equilibrium MD simulations served to infer the time series of a number of geometric descriptors including the solvent accessible surface area (SASA), the intrinsic flexibility (*i.e.*, the Cα-atom root mean square fluctuations (RMSFs)), and the essential motions of the proteins by the principal component analysis (PCA) of the atomic fluctuations, and to extract representative frames for docking simulations with intracellular proteins. For each receptor form, ensembles of maximum 400,000 conformations saved every ps were analyzed by the Wordom software [27,28].

Rigid-body docking simulations between the receptor and the intracellular proteins were carried out by means of the Z-dock 3.0.2 software [29], whereas docking post-processing was done by the FiPD software [30]. Selected structures of the H2- and H6-variants from the MD trajectories as well as the available crystal structures of the two H2-variants, G90D (PDB: 4bez and 4bey, [18]) and T94I (PDB: 5dys and 5en0, [19]) were subjected to docking simulations with the mini Gi (mGi: sequence 1–53 and 183–354) or ARR1 (sequence: 12–362) extracted from the Cryo-EM complexes with active opsin (PDB: 6cmo [31] and 5w0p [32], respectively). The mGi from the 6cmo complex was obtained by deleting the helical domain. The mGi extracted from the complex with MII (PDB: 6qno [33]) was probed as well. The RHO protein was used as a fixed target, whereas mGi and ARR1 were used as probes. All known cryo-EM complexes between the RHO receptor (in the opsin or MII states) and Gt, Gi, or ARR1 were reconstituted to probe the methodology. Because no high-resolution structural model has been released so far, docking simulations were carried out to build the complex between WT RHO MII (PDB: 3pxo) and ARR1. In all docking runs, a dense rotational sampling was set. The best 4000 solutions from each run were filtered according to the distance (12 Å) between the Cα-atom of R135 of RHO and either L353 in the C-term of mGi or L78 in the finger loop of ARR1. The filtered solutions were subjected to cluster analysis (with a Cα-RMSD cutoff = 2 Å) followed by visual inspection of the cluster centers as in [30]. From each docking run, the most native-like solution was selected. In detail, a docking solution was considered as native-like if the inter-protein interface held a Cα-RMSD $\leq$2.5 Å with respect to the high-resolution complexes. The receptor-mGi interface in 6cmo and 6qno was considered for the opsin-mGi and MII-mGi complexes, respectively, whereas the receptor-ARR1 interface in 5w0p and in a complex modeled by docking ARR1 onto MII was considered for the opsin-ARR1 and MII-ARR1 complexes, respectively. The interface-residues employed to compute the Cα-RMSD of the native-likeness were those holding at least one atom at 7 Å distance from any atom in the interacting partner. The maximal number was taken from the analysis of all predicted complexes and the gaps made by few amino acids were filled. The final amino acid selections were the following: a) for RHO-mGsi, RHO: 67–73, 131–152, 223–257, and 305–313, mGsi: 27–32, 193–195, 308–321, and 334–354; b) for RHO-ARR1, RHO: 66–74, 131–151, 222–254, and 306–316 and ARR1: 66–88, 126–145, 160–164, 248–256, 292–293, and 319–322.

In the opsin-ARR1 bound state, intracellular loop 2 (IL2) holds a two-turn helix, while it is in random conformation in the isolated and G protein-bound states. MD simulations suggest that such helix can form, but rarely, in the isolated states. ARR1 binding likely selects structures with the IL2 in helical conformation. Based on this evidence, for docking simulations with ARR1, the crystal structures of WT MII (PDB: 3pxo), G90D (opsin) and T94I (MII) and, for all other forms, the frames closest to the opsin structure in the 5w0p complex were used with their IL2 in the original random conformation or with IL2 in ARR1-bound helical conformation, upon mounting the IL2 extracted from the 5w0p complex. All docking simulations produced native-like complexes, but the best-scored and native-like complexes were achieved when IL2 holds two-turn helix. The results that are shown herein concern the latter conditions.

The selected complexes were subjected to the PSN analysis by the PSNtools software [34]. Briefly, PSN analysis is an application of the graph theory to protein structures. In a protein structure graph, each amino acid is a node and pairs of nodes are connected between each other if the strength of the non-covalent interaction is higher than a cutoff. Nodes involved in at least four links are defined as hubs. The analysis of receptor-mGi and receptor-ARR1 interfaces relied on the interaction strength of those WT links (native links) involving at least one hub (Hlinks) in the interface of the opsin or MII receptor forms. In the four variants of RHO (G90D, T94I, W265R, and A269V) the force of a native Hlink was set to zero if neither one of the two linked nodes behaved as a hub.

2.4. cDNA constructs

WT *RHO* cDNA in the pRc/CMV expression vector [12] was used for site directed mutagenesis to generate the W265R, A269V, G90D and T94I adCSNB variants. Q5 Site-Directed Mutagenesis Kit (NEB) was used to introduce the desired base change with specific primers (Table 2), following manufacturer's instructions. The mutagenized cDNAs were checked by Sanger sequencing.

For BRET experiments, WT and mutant *RHO* cDNAs were cloned in the mammalian expression plasmid pcDNA3.1-Rluc8 using *Nhe*I/*Bam*HI restriction sites. In order to link in frame at the C-term the WT and mutant RHO to Renilla Luciferase (Rluc8), the stop codon was removed at the 3′ end of *RHO* cDNA. The open reading frames of RHO-Rluc8 in pcDNA3.0-RHO-Rluc8 were checked by sequencing.

The cDNA encoding truncated ARR1 (tARR1), containing amino acids 1 to 378, was amplified from human retina cDNA using specific primers:

h-SAG-Fw - CCATGGCAGCCAGCGGGAAGAC;
h-SAG1-378-Rev - CGGGATCCAACTAAATTTGCATCCTGATAACTTTCC

Table 2
Primers used for site-directed mutagenesis.

Mutation	Forward primer[a]	Reverse primer
G90D	GTCCTAGGTG**A**CTTCACCAGC	CATGAAGAGGTCAGCCAC
T94I	TTCACCAGCA**T**CCTCTACACC	GCCACCTAGGACCATGAA
W265R	CCTGATCTGC**C**GGGTGCCCTA	AAAGCGATGACCATGATGATGAC
A269V	GTGCCCTACG**T**CAGCGTGGCA	CCAGCAGATCAGGAAAGCGATGACC

[a] Bold and underlined letters represent the mutagenized base.

and cloned into pcDNA3.0-YFP using *Nhe*I/*Bam*HI restriction sites to generate the construct pcDNA3.0-tARR1-YFP with tARR1 in frame with YFP. The plasmid pVenus-C1, containing miniGsi (NES-Venus-mGsi) in frame with the *Venus* cDNA, was used for miniGsi (mGsi) expression [35].

2.5. In vitro subcellular localization analysis

WT or mutant RHO in the pRc/CMV plasmids were transfected in COS-7 cells (CRL-1651, ATCC) using Escort III transfection reagent (Sigma Aldrich). Cells were treated with either 10 μM 11-*cis*-retinal (Sigma Aldrich) or 9-*cis*-retinal (Sigma Aldrich) or vehicle (dimethyl sulfoxide, DMSO; Sigma Aldrich) 24 h after transfection.

ER and plasma membrane localizations were analyzed as previously published [12]. Briefly, ER localization of RHO protein was detected with the 1D4 mAb (1:500; Sigma Aldrich), which binds an intracellular epitope at the C-term of RHO, and with α-CLNX (1:100; StressMarq Biosciences), which identifies the ER resident protein calnexin (CLNX). RHO at the plasma membrane was visualized, in the absence of cell permeabilizing agents, with RetP1 mAb (1:500; Thermo Fisher), which binds an extracellular epitope at the N-term of RHO. Images were acquired at a Zeiss Axio Imager A2 microscope with Zen Blue Software and co-localization analyses based on PCC were performed with Fiji (ImageJ, National Institute of Health, Bethesda, MD, USA) as previously described [12]. PCC values can range from 1 to −1, where a value of 1 represents perfect correlation, value of −1 is perfect but inverted correlation and values near zero represent distributions of fluorescent signals that are uncorrelated (Dunn et al., 2011).

For the evaluation of RHO localization at the plasma membrane, the number of cells labelled at the extracellular N-term in the absence of membrane permeabilization ($RetP1^+$) was divided by the number of transfected cells expressing RHO in any cellular compartment and visualized after membrane permeabilization ($1D4^+$).

2.6. cAMP assay

COS-7 cells were seeded at the concentration of 20,000 cells per well in 96 well plates in technical duplicates for each condition. Cells were transiently transfected with Metafectene PRO (Biontex Laboratories GmbH) in suspension with 100 ng of pcDNA3.0-RHO-WT-Rluc8 plasmid and with 100 ng of pcDNA3.0-Gi-YFP plasmid encoding a Gi protein in frame with YFP [35]. 48 h after transfection, cells were treated as follow: 20 min of pre-incubation with 500 nM 3-isobutyl-1-methylxanthine (IBMX; Sigma Aldrich), phosphodiesterase enzymes inhibitor, followed by 15 min of incubation with 500 nM IBMX and 10 μM 9-*cis*-retinal or DMSO (vehicle) and 5 μM coelenterazine h (CTZh; NanoLight Technologies). Cells were then treated with 5 μg/ml cholera toxin to activate Gs (Sigma Aldrich) and lysed by freeze-thaw. cAMP in the lysate was quantified by Detect X Direct Ciclic AMP ELISA kit (Arbor Assays) following manufacturer instructions. Absorbances were measured at 450 nm with the GlowMax Discover System (Promega).

2.7. Bioluminescence Resonance Energy Transfer (BRET)

To assess coupling of RHO to Gα protein we co-expressed RHO-Rluc8 (WT or adCSNB variants) with mini Gsi (mGsi), a G protein that had been developed to test GPCR-G protein coupling using BRET [35]. mGsi was chosen because RHO had been previously crystallized with a miniG protein, containing only the ras domain [36].

pcDNA3.0-RHO-Rluc8 and either NES-Venus-mGsi or pcDNA3.0-tARR1-YFP were transiently transfected in COS-7 cells using Metafectene PRO (Biontex Laboratories GmbH). In order to evaluate the best transfection condition for BRET experiments, we tested 25, 50 or 100 ng of plasmids expressing the different RHO variants and different amounts of either NES-Venus-mGsi or pcDNA3.0-tARR1-YFP and 100 ng of pcDNA3.0-RHO-Rluc8 was selected as optimal amount for RHO expression. Transfections for BRET assays were performed in a final volume of 50 μl/well of transfection mixture containing 100 ng of pcDNA3.0-RHO-Rluc8 (either WT or mutant RHO) and increasing amounts of NES-Venus-mGsi or pcDNA3.0-tARR1-YFP plasmids (0 to 400 ng). For coupling analysis, 48 h after transfection, cells were incubated in serum-free medium for 24 h with either DMSO (vehicle) or 10 μM 9-*cis*-retinal, the chromophore. 72 h after transfection, cells were exposed to 5 μM CTZh, the Rluc8 substrate, and light emissions from Rluc8 (480 nm) and YFP or Venus (530 nm) were detected with a CLARIOstar plate reader (BGM Labtech).

Based on data collected from coupling experiments, BRET experiments in kinetics were performed on COS-7 cells transfected with 100 ng/well pcDNA3.0-RHO-Rluc8 and 100 ng/well of either NES-Venus-mGsi or pcDNA3.0-tARR1-YFP (ratio 1:1). 48 h after transfection, Rluc8 and YFP or Venus emissions were measured with a CLARIOstar plate reader every 3 s for a total time of 30 min. After the first 10 min, either 10 μM 9-*cis*-retinal or control vehicle (DMSO) were added to each well and light emissions were recorded in real time for the remaining 20 min. BRET data derive from 4 different biological replicates.

2.8. Data analyses

We performed at least four biological replicates for each experiment and data are represented as the mean ± standard error of mean (SEM). For the analysis of membrane/total RHO and ER localization, One-Way ANOVA with Šidàk's multiple comparison test was applied using GraphPad Prism 9.0 and $p \leq 0.05$ was considered significant. For BRET coupling and kinetics experiments, the Area Under the Curve (AUC) was measured for each RHO variant, and AUC of 9-*cis*-retinal treatment were compared to vehicle treated samples using the Mann-Whitney's *U* test.

3. Results

3.1. Identification of two novel pathogenic RHO variants in adCSNB patients

We identified two French families (families 1 and 2) with novel missense pathogenic variants in *RHO*, c.806C>T (p.A269V) and c.793T>C (p.W265R), respectively. The four-generation family 1 presented typical Riggs-type of CSNB segregating as an autosomal dominant trait (Fig. 1A). The index patient (III:2) and her daughter (IV:3) complained about non-progressive night blindness with normal day vision since early childhood. The index patient's daughter (IV:3) was not available for an ophthalmic examination but the index patient (III:2) was clinically investigated. The 50-year-old index patient reported signs of nyctalopia since childhood and photophobia since the age of 45 years.

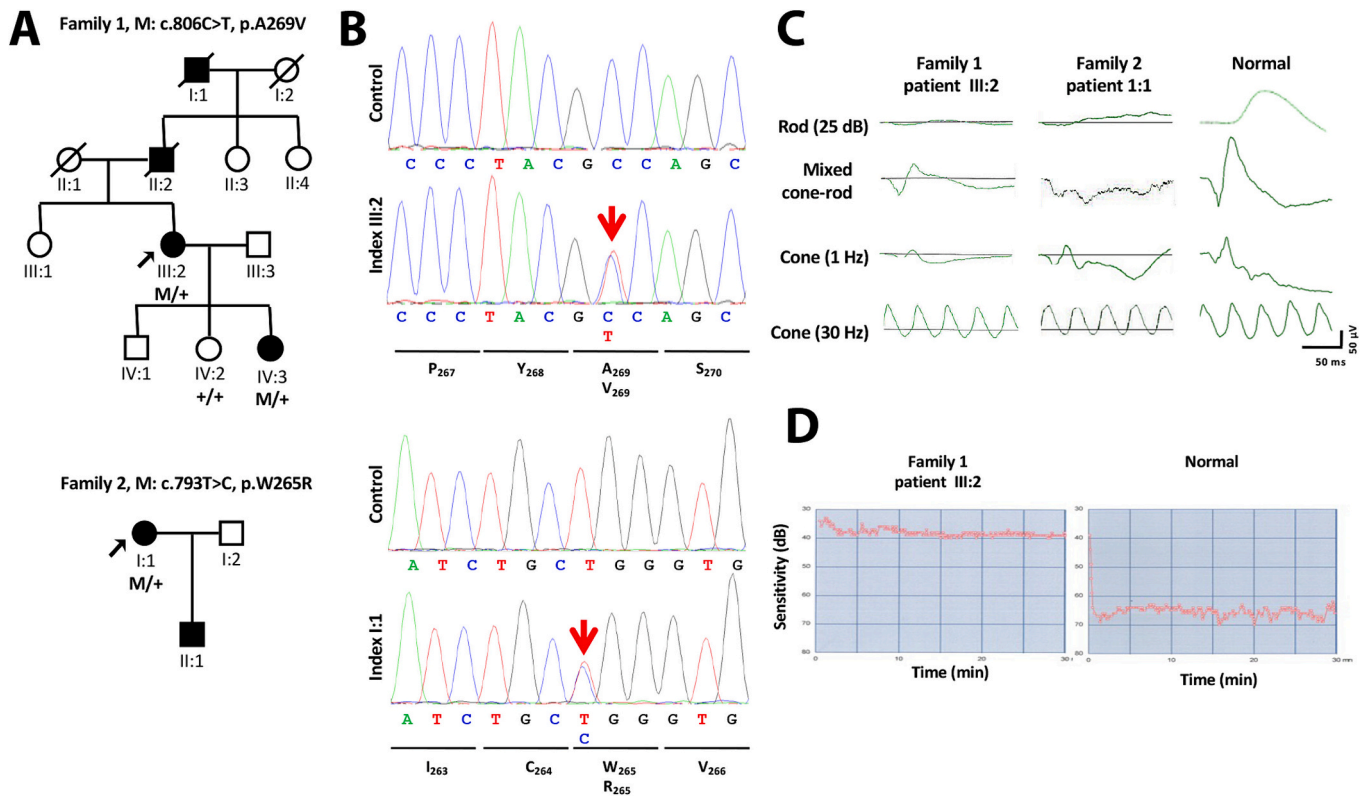

Fig. 1. Pedigrees and clinical characterization of adCSNB patients. (A) Pedigrees of families 1 and 2 with adCSNB. Filled symbols indicate affected family members; squares: males; circles: females; arrow: index patient; slashed symbols: deceased persons. M indicates the presence of the pathogenic variant and + indicate the WT allele. (B) Electropherograms show the normal control sequence and affected sequence (index individuals, red arrow) surrounding the *RHO* pathogenic variants. (C) Full-field ERGs from normal control and index patients III:2 (family 1) and I:1 (family 2). (D) Dark-adaptation curve of index patient III:2 (family 1) compared to normal curve. (For interpretation of the references to color in this figure legend, the reader is referred to the web version of this article.)

Her best corrected visual acuity was 20/20 on both eyes. The fundus showed no sign of retinal degeneration as the posterior pole, macula, and optic discs had normal appearance except for a discrete peripapillary atrophy related to myopia. The retinal vessels were not attenuated. The fundus autofluorescence (FAF) and the spectral-domain optical coherence tomography (SD-OCT) were normal. The ERG profiles of the index patient and a representative control subject are shown in Fig. 1C and D. Scotopic ERGs, that assesses rod photoreceptor functionality, was severely reduced but recordable. Photopic ERGs and 30-Hz-flicker ERG, that primarily assess cone photoreceptor functionality, did not show alterations (Fig. 1C). Dark adaptometry revealed a total absence of rod adaptation at 30 min and a weak adaptation of the cones (Fig. 1D).

In family 2, the index patient (I:1) complained about non-progressive night blindness with normal day vision since early childhood. At presentation, the 37 year-old index subject had neither visual field loss nor photophobia and had normal visual acuity at 20/20 in both eyes. The fundus and FAF examinations of the index patient were normal. The ERGs showed the absence of rod responses while the cone responses were normal (Fig. 1C). The dark adaptometry test could not be performed for the index patient in family 2. The son of the proband (II:1), 3-year-old, was too young for a complete ophthalmic examination but also presented signs of night blindness.

Direct sequencing of the three known genes underlying adCSNB of the index patients of families 1 and 2, revealed a heterozygous c.806C>T variant resulting in a p.A269V alteration and a heterozygous c.793T>C variant resulting in a p.W265R alteration in *RHO* (NM_000539.3), respectively. Both variants were in exon 4. No disease-causing variants in *PDE6B* and *GNAT1* were detected. The p.A269V variant co-segregated with the phenotype in all available members of family 1 (Fig. 1A and B). DNA was not available for sequencing from other members of family 2. Both variants were absent from the human public database gnomAD and were predicted to be damaging by all the pathogenicity prediction software used (Table 1; PolyPhen2, SIFT, Provean, align-GVGD, REVEL, CADD and Varsome).

3.2. Structural effects of the adCSNB variants on the RHO protein

The structural effects of the adCSNB-linked W265R and A269V variants were first analyzed *in silico*. The amino acid residues W265 and A269 lie on the extracellular half of H6 two positions upstream and downstream of the highly conserved P267 residue, which confers functionally important conformational degrees of freedom to the helix (*e.g.*, a kink in the inactive state of the receptor). In the dark state structure of RHO, W265 makes van der Waals interactions with the β-ionone ring of 11-*cis*-retinal. Such interactions are lost in the photoactivated states, due to the all-*trans* isomerization of the chromophore. Arginine substitution for W265 induces the formation of a salt bridge with E122 on H3 (Fig. 2). Such salt bridge persists in all frames of equilibrium MD simulations of the W265R mutant in both the opsin and MII states. A269V faces both F208 and F212, situated six and two positions upstream of the conserved P215, and causes a peculiar deformation in H5 (Fig. 2), altering local H5-H6 packing interactions. The local perturbations induced by the two H6-variants differ significantly from the two H2-variants, G90D and T94I, which perturb the Schiff base by salt bridge or van der Waals interactions with K296 (Fig. 2).

The α-helix containing W265 and A269 is central in the process of RHO activation, which is characterized by conformational changes in H5 and outward movements of H6, coupled to breakage of the dark RHO salt bridges between R135, of the E/DRY motif, and E134 and E247 [37]. Such structural changes favor the formation of a binding site for Gt, participated by the cytosolic extensions of H3 (containing R135), H5 and H6, the N-term of H8, the three intracellular loops (IL) and the C-

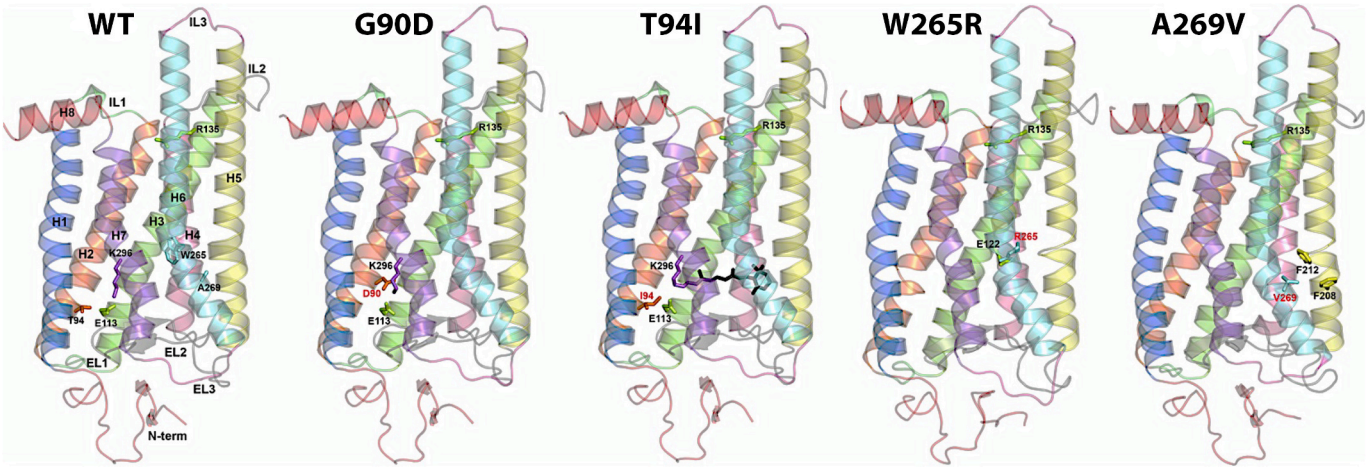

Fig. 2. Structural models of adCSNB variants in RHO. Side view, in a direction parallel to the membrane surface, of the crystal structures of WT (pdb: 3cap), G90D (PDB: 4bez) and T94I (PDB: 5dys), and of two frames of W265R and A296V from molecular simulations. The cytosolic side is at the top. H1, H2, H3, H4, H5, H6, and H7 are colored in blue, orange, green, pink, yellow, cyan, and violet, respectively; N-term and C-term, the latter including H8, are red, IL1 (intracellular loop 1) and EL1 (extracellular loop 1) are lime, IL2 and EL2 are grey, and IL3 and EL3 are magenta. The all-*trans*-retinal, present only in T94I, is shown in black sticks. Mutation sites, mutated side chains and surrounding amino acids are represented in sticks. (For interpretation of the references to color in this figure legend, the reader is referred to the web version of this article.)

term [26,31,38]. ARR1 competes for the same Gt-protein binding site on RHO [32].

We first investigated if the two novel H6-variants could cause misfolding of mutant opsin. To this end, we exploited a computational model based on unfolding simulations and PSN analyses that we developed for 39 adRP RHO mutants [22]. In that model, the mutation-caused structural perturbations compared to the WT were expressed in terms of native hubs (*i.e.* nodes involved in at least four links) and their links with reduced frequency over the simulation time. Hub and hub-link weakening were translated into a network perturbation (NP) index that linearly correlated with the PCC index of ER retention calculated by expression of the RHO mutants *in vitro* (Fig. 3A and B). The W265R and A269V NP indexes (25.26 and 22.56, respectively) in the presence of 11-*cis*-retinal indicated no misfolding. The NP index was, then, used to predict their PCC, *i.e.* 0.45 and 0.42, respectively, which suggested no or minimal of ER retention when bound to retinal. The analysis of the hub-mediated retinal-mediated sub-network (*i.e.*, the stable native network mediated by hubs in the first and second interaction shell of retinal), otherwise, showed slight perturbation and weakening of the Hlinks, which were more evident in W265R compared to A269V (Fig. 3C and D). This suggested that the H6-variants, in particular W265R, although non-misfolded might be perturbed in the retinal binding site.

Based on the *in silico* studies, we assessed whether H2- and H6-variants disturbed plasma membrane localization. The subcellular localization of G90D and T94I, did not significantly differ from WT RHO in the presence or absence of 11-*cis*-retinal (Fig. 3E-G). Colocalization analysis of the two novel H6-variants with CLNX, an ER resident protein, highlighted slight retention in the ER of A269V in absence of retinal (PCC = 0.56 ± 0.12, $^{*}P < 0.05$), whereas W265R behaved as WT (PCC = 0.5 ± 0.10) (Fig. 3F-G). The exposure to 11-*cis*-retinal restored localization of A269V to a value similar to WT (PCC = 0.51 ± 0.09), but, interestingly, slightly increased retention in the ER of W265R (PCC = 0.58 ± 0.11, $^{**}P < 0.01$, Fig. 3F and G). The effect of retinal on ER retention of W265R might be related, at least in part, to Hlink perturbations in the retinal binding site, as inferred from PSN analysis and not present for the A269V variant (Fig. 3C and D). Overall, these data showed that the adCSNB variants are not majorly misfolded and could reach the plasma membrane.

We then inferred the effects of H2- and H6-variants on the intrinsic dynamics of RHO by analyzing the conformational ensemble from equilibrium MD simulations of the active opsin and MII forms. The fluctuations of the Cα-atoms deduced from the Cα-RMSF profiles suggested that, for all variants in both states, the most flexible regions are the N-term, IL2, IL3, the cytosolic protrusions of H5 and H6, EL3, and H8 (Fig. S1A). In the opsin state, the H6-variants show higher flexibility of the H5-IL3-H6 portion compared to the MII state of the same variants and both states of the H2-variants (Fig. S1A and B). Moreover, in the opsin state, both H2- and H6-variants show increased flexibility of H8, which is higher than the respective MII states (Fig. S1A and B). This observation clearly emerges from the Cα-RMSF profiles averaged over the two states of the H2- or H6-variants and mapped onto the 3D structures (Fig. S1C and D). In line with fluctuation profiles, the analysis of collective motions by the PCA of the Cα-atom fluctuations showed that the first three principal components (PC) describe collective displacements of IL2, IL3, the cytosolic extensions of H5, H6 and H8, that likely deform the G protein and ARR1 binding sites. Such deformations were associated to changes in the SASA indexes of selected cytosolic amino acids: L72, Y74, R135, V139, T251, I255, K141 and M309. SASA index is a hallmark of the inactive and signaling active states of RHO: 269.47 ± 38.44 $Å^2$ for the crystal structures of dark RHO (PDB: 1u19, 1gzm, and 2ped) and 620.95 ± 29.39 $Å^2$ for the structures of activated RHO, either in the isolated state or in complex with G protein/arrestin (PDB: 3cap, 5w0p, 6cmo, 6oy9, 6oya, and 6qno). For the crystallographic structures of G90D opsin and T94I MII the SASA indexes were 610.00 $Å^2$ and 602.52 $Å^2$, respectively. As for the conformational ensembles of the H2 and H6 variants, in the opsin and MII states, we calculated a median SASA index of 535.57 ± 46.37 $Å^2$ (Fig. S2).

Altogether, these analyses suggested that, by different ways and extents, mutations in H2 and H6, while not misfolding, affect the dynamics of the cytosolic crevice involved in G protein/arrestin interaction.

3.3. RHO coupling to G protein is affected in adCSNB variants

Based on MD simulations, we probed the propensity of the adCSNB variants to interact with the G protein (mGi, see Methods) by docking simulations. For all predicted complexes, the interface Cα-RMSDs between predicted and native complexes were significantly lower than the 2.5 Å cutoff, chosen to define an interface as a native-like. Collectively, these results suggested that the four considered variants were able to form native-like complexes with the G protein. The receptor-mGi

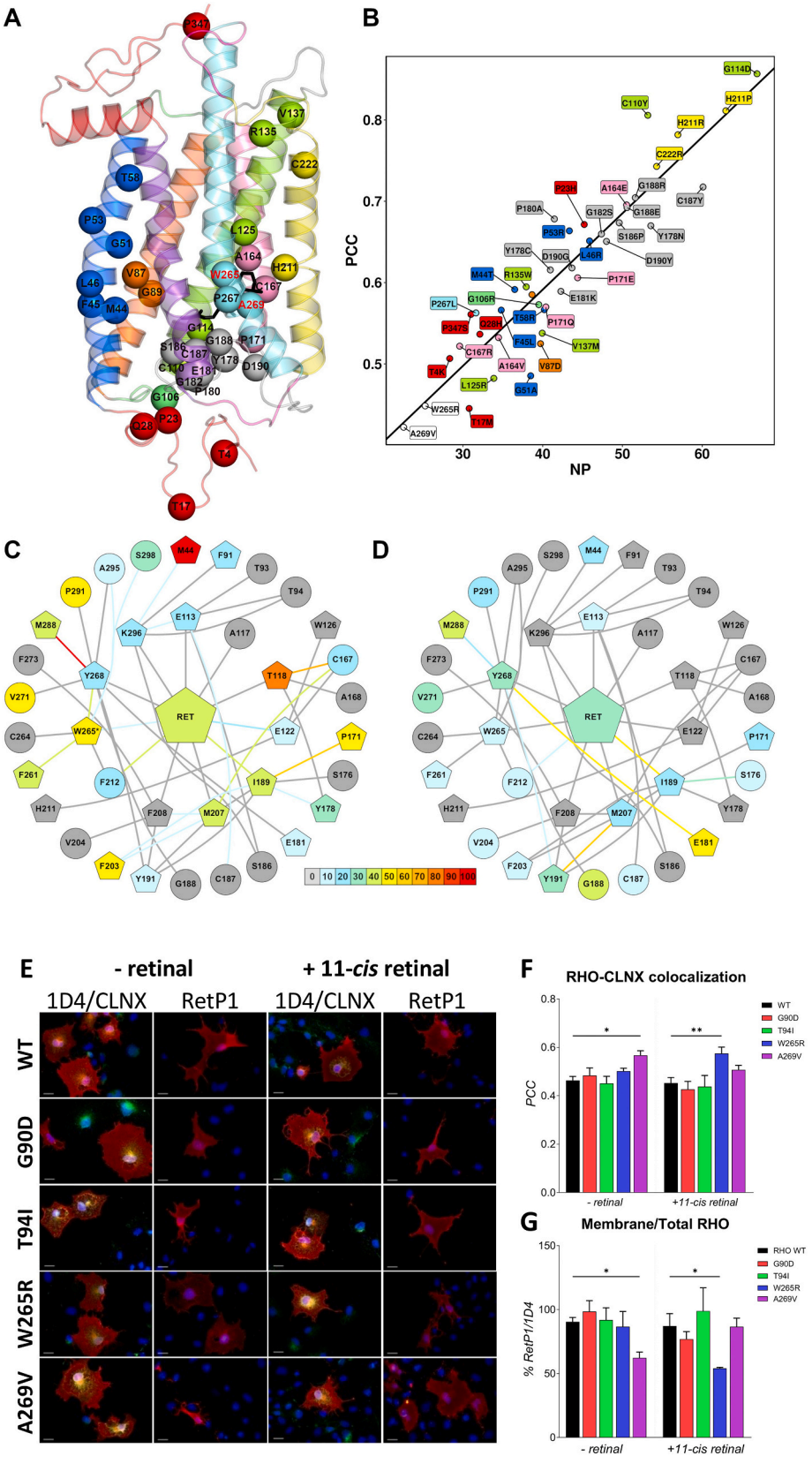

(caption on next page)

Fig. 3. Assessment of misfolding of adCSNB variants. (A) The mutation sites on the structure of RHO are represented as spheres centered on the Cα-atoms on the crystal structure of dark RHO (PDB: 1u19). While the majority of the spheres concerns the adRP mutation sites used to calibrate the computational model, the two spheres with the red labels concern the novel adCSNB variants in H6 (cyan). (B) The scatter plot shows the linear correlation between the NP index accounting for mutational effects on the native structure network and the PCC index accounting for ER retention. Low NP index denotes no or minimal effects on structure network, low PCC index indicates no or low ER retention. Dots are colored according to the amino acid structural location, as shown in panel A. The two H6-variants linked to adCSNB are shown in white. (C-D) The 2D-networks concerning hubs (pentagons) and their links in the retinal-binding pocket (RET = 11-*cis*-retinal) of WT RHO are shown. Coloring of links and nodes indicates the perturbation caused by W265R (C) or A269V (D) as depicted in the color legend. The color of each hub represents the percentage of perturbed hub-links (*i.e.*, with reduced frequency with respect to the WT). Each link is colored according to its perturbation compared to the WT. The asterisk on the W265 means that such native hub is replaced by arginine in the considered mutant. A269 is not a hub and thus not shown in the fig. (E) Micrographs of immunofluorescence analyses of WT and mutant RHO (1D4, red) and the colocalization with ER marker CLNX (green) in the presence or absence of 10 μM 11-*cis*-retinal (1D4/CLNX). Membrane localization of RHO WT and adCSNB variants was assessed with RetP1 antibody in the absence of plasma membrane permeabilization (RetP1). (F) Histogram representing PCC values of RHO-CLNX colocalization. (G) Histogram shows the quantification of WT and mutant RHO at the plasma membrane based on the ratio of the number of cells presenting RHO at the plasma membrane ($RetP1^+$) *versus* total number of transfected cells ($1D4^+$). (One Way ANOVA; $^*P < 0.05$; $^{**}P < 0.01$). (For interpretation of the references to color in this figure legend, the reader is referred to the web version of this article.)

interface in the most native-like complexes underwent PSN analysis, focusing on those links that characterize the reference complexes between mGi and WT active opsin or MII (*i.e.*, native links). The native links involving at least one hub node (*i.e.*, Hlinks) turned out to be proper reference frames to infer the effects of the H2- and H6-variants on mGi coupling. In fact, hubs are hyperlinked nodes and the hot spots in protein-protein recognition often fall in densely packed regions (hot regions) of interfaces [39]. Indeed, the total force of the interface native-Hlinks was able to distinguish the opsin and MII states of RHO in complex with mGi (Fig. 4).

In the native complexes between opsin/MII and mGi, the C-terminal helix (α5) of the G protein docks onto a cavity participated by H2, H3, H5, H6, and H8 of RHO, whereas the N-terminal helix (αN) and the β6-strand with IL2 and IL3 of RHO, respectively (Figs. 4A and S3A). PSN analysis of the receptor-mGi interface showed that the distribution of the 22 native Hlink-nodes in mGi was the following: 15 (68 %) in α5, 5 in β6, and 2 in αN, with two interface hot regions participated by β6 and α5 of mGi (Figs. 4 and S3A and Table S1). The total interaction strength of the interface native Hlinks was 64.66 % and 114.41 % for the native complexes involving opsin and MII, respectively (Fig. 4A and B), suggesting that the index could roughly mark receptor-G protein coupling effectiveness. On these bases, the index was employed to investigate the effects of the H2- and H6-variants on the RHO-mGi interface in the absence and presence of all-*trans*-retinal. In the opsin states and MII states, the indexes were higher in the H6-variants when compared to the H2-variants (Fig. 4B and C, Table S1). Otherwise, the difference between MII and opsin states (ΔHlinks) highlighted the following trend: T94I > WT > G90D > A269V > W265R (Fig. 4B-D). H6-variants had negative ΔHlinks, indicating better coupling in the opsin state than in the MII state. In summary, in the opsin states and compared to WT, the H6-variants displayed stronger coupling with mGi than the two H2-variants. On the contrary, in the MII states and compared to the opsin states, the WT and the two H2-variants, in particular T94I, improved their coupling while the two H6-variants slightly worsen their interaction with mGi (Fig. S4).

To experimentally confirm the *in silico* finding we assessed RHO coupling to G protein by BRET. The assay was based on co-expression of RHO linked at the C-term to Rluc8 together with a mGsi protein linked to Venus (see Methods for details).

To define whether the BRET technique could be appropriate to test binding of RHO to the G protein α subunit, we verified if, in the presence of CTZh, the substrate of Rluc8, emission of visible light by the enzyme could isomerize 9-*cis*-retinal and activate RHO. In this assay we chose to test interaction of WT RHO with Gi because Gt is a Gi/o subfamily member [40] and RHO was previously shown to bind Gi [31]. Besides, the assay with Gi provided us with a measurable outcome, which was the concentration of the second message cAMP. To this purpose, COS-7 cells co-transfected with RHO-Rluc8 and Gi protein linked to YFP were treated with the chromophore 9-*cis*-retinal and CTZh. Gi-YFP is a construct similar to the one used for BRET assay (mGsi) but contains the entire Gi necessary for interaction and inactivation of adenylate cyclase. Samples co-expressing RHO and Gi and treated with 9-*cis*-retinal, upon exposure to CTZh, displayed reduced levels of cAMP (Fig. S5), demonstrating that visible light emitted by Rluc8 could activate RHO, which, in the artificial system based on expression of Gi, transduced the signal and caused inhibition of the adenylate cyclase and decrease of intracellular levels of cAMP.

Coupling of the RHO-RLuc8 with the G protein was then tested by adding increasing amounts of Venus-mGsi. BRET saturation curves were obtained for WT RHO and adCSNB variants both in the presence and absence of 9-*cis*-retinal, indicating specificity of interaction (Figs. 5 and S6). The specificity of the coupling was confirmed by the left-shifted coupling curve, as well as higher plateau levels, of RHO WT in presence of 9-*cis*-retinal (Figs. 5A and S6B, green lines). These observations suggested that RHO could be reconstituted with 9-*cis*-retinal and, upon light emission from Rluc8, activated and enabled to bind the mGsi. BRET saturations curves highlighted different ratios of protein-protein interaction among the adCSNB variants when compared to WT RHO. Specifically, we observed a higher interaction with mGsi of H6-variants in the absence of retinal compared to WT RHO (Fig. 5A and D-F, black curves), which suggested constitutively activated conformations of W265R and A269V variants. In contrast, H2-variants were characterized by lower binding to mGsi in the absence of retinal (Fig. 5A-C, black curves, and F). While H2-variants increased their interaction with mGsi in the presence of the 9-*cis*-retinal, the novel pathogenetic H6-variants, in this same condition, displayed equal or reduced coupling with mGsi, as accounted for by the difference in BRET area under curve (ΔAUC) between MII, stimulated with retinal and light, and opsin states, in the absence of retinal (Fig. 5G). Remarkably, those trends were consistent with the results of docking simulations (Fig. 4). In fact, for both the opsin and MII states, the BRET calculated AUC linearly correlated with the Hlink interaction strength ($R^2 = 0.94$ and $R^2 = 0.92$, respectively) (Fig. S7).

For a longitudinal analysis of RHO binding with the G protein over time and to finely measure the rate of interaction between the RHO-Rluc8 and Venus-mGsi after isomerization of 9-*cis*-retinal, we performed coupling kinetics. RHO WT coupling with mGsi reached the plateau at 400 s after treatment with 9-*cis*-retinal, while slower kinetics were observed for all adCSNB variants (Fig. 6A-E). Specifically, G90D had a right-shifted peak, indicating slower interactions with mGsi when compared to WT RHO (Fig. 6B). Similarly, T94I had slower coupling to mGsi than WT, although the interaction constantly increased over time reaching levels higher than WT RHO (Fig. 6C). Differently, no significant change in coupling of W265R and A269V variants with mGsi could be detected upon exposure to 9-*cis*-retinal (Fig. 6D and E). To quantify these results, we calculated the AUC in the presence and absence of 9-*cis*-retinal for WT RHO and each variant and confirmed higher coupling to mGsi of T94I than WT, while no interaction changes of W265R and A269V was induced by retinal (Fig. 6F).

In summary, molecular simulations and coupling experiments highlighted that H6-variants are prone to constitutively couple to the G protein and suggested that these variants may maintain an activated

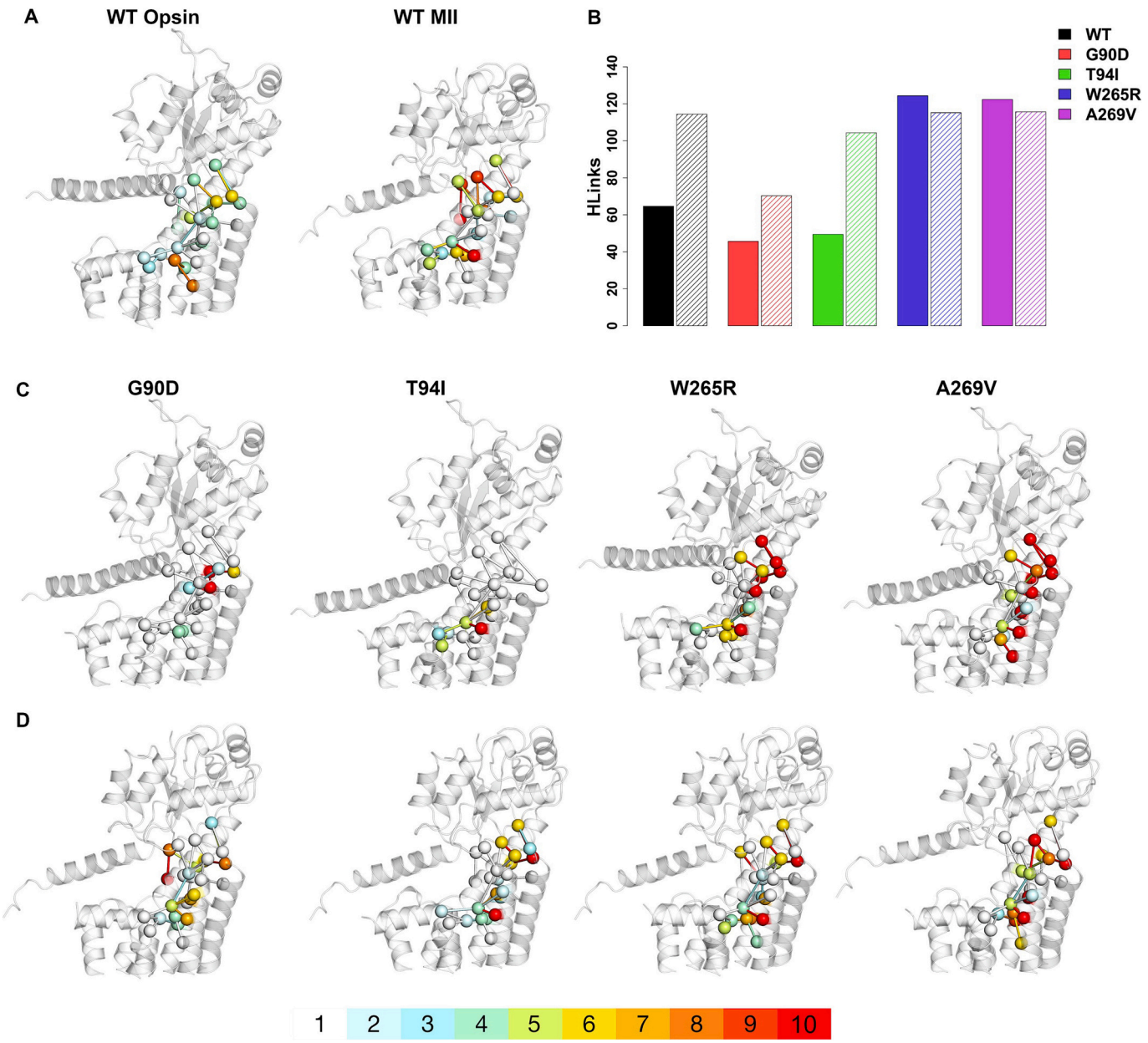

Fig. 4. PSN analyses of the predicted interfaces in the complexes between the adCSNB variants and mGi. (A) Cartoon representations of the cryoEM structures of the complexes of WT opsin (left) and WT MII (right) with mGi (PDBs: 6cmo and 6qmo, respectively) in which the extracellular halves of the receptors are not shown. The native interface-Hlinks and the involved nodes are shown. Links are colored according to their interaction strength (see the color legend at the bottom of the figure) whereas nodes are colored according to the average interaction strength of the links they are involved in. (B) Histograms of the summations of the interaction strength of all interface native Hlinks for the opsin (filled histograms) and MII (dashed histograms) states for WT (black), G90D (red), T94I (green), W265R (blue), and A269V (violet). (C-D) The predicted complexes between the opsin forms (C) and MII forms (D) of G90D, T94I, W265R, and A269R and mGi are shown. The native interface-Hlinks and the involved nodes are colored according to the interaction strength. (For interpretation of the references to color in this figure legend, the reader is referred to the web version of this article.)

state when retinal is released upon light stimulation. Differently, H2-variants displayed a slow binding to G protein, with T94I strongly increasing the coupling with mGsi when activated.

3.4. Effects of adCSNB variants on coupling of RHO with ARR1

The PSN-based approach employed to analyze the RHO-mGi interfaces was applied to the RHO-ARR1 complexes. In the native complex between RHO opsin and ARR1 (PDB: 5w0p) the phosphorylated C-term of the receptor interacts with the N-terminal domain of ARR1 forming the interface-1, whereas the other cytosolic portions of the RHO form the interface-2. The latter is contributed by IL1, IL2, H2, H3, H5, H6, and H8 of RHO and finger loop, C-loop and β-strands 5, 6, 9, 15, and 16 of ARR1 (Fig. S3B). The finger loop of ARR1 docks in the same receptor site as the α5-helix of the G protein (Fig. S3A and B). It is worth noting that the structural models of RHO used herein lacked the C-term, therefore, only interface-2 was considered in the analysis. The best predicted RHO-ARR1 complexes, held an average RMSD from the experimental interface equal to 1.17 Å (Fig. S8). PSN analysis of the predicted interface showed 17 out of 28 (61 %) Hlinks involving the region 66–83, which comprises the finger loop and the N-terminal portion of β6 of ARR1 and H3, H5, H6, H8, IL2, and IL3 of RHO (Table S2, Figs. 7 and S3B). Native Hlinks formed approximately two hot regions at the interface of the complexes between ARR1 and WT opsin/MII. One hot region was

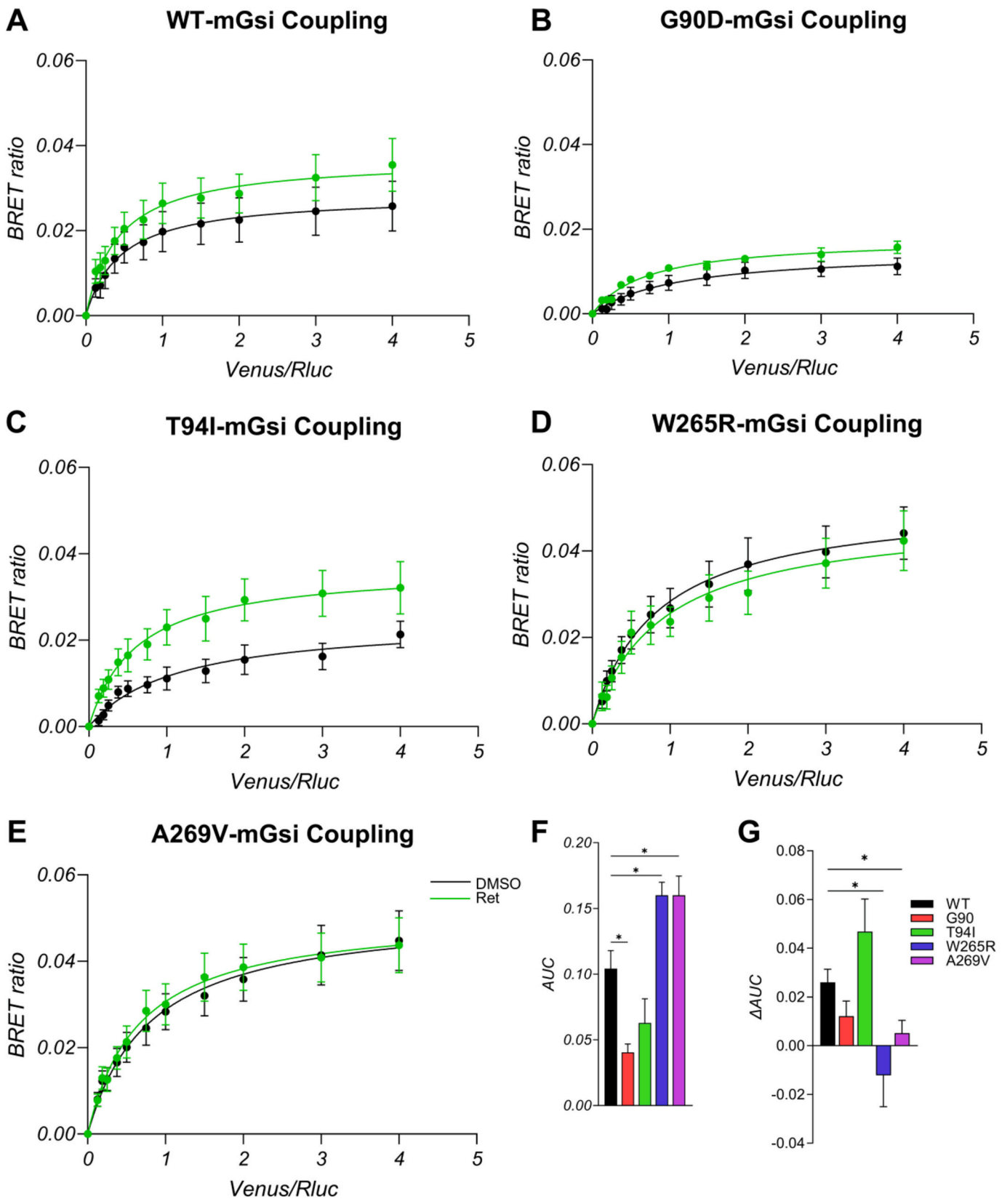

Fig. 5. Coupling analyses of RHO variants with mGsi by BRET. (A-E) Coupling of RHO WT and adCSNB variants with mGsi was assessed by BRET in the presence (Ret, green lines) or absence (DMSO, black lines) of 9-*cis*-retinal. (F) Histogram of the Area Under the Curve (AUC) quantified from the BRET signals of samples treated with vehicle (black lines in A-E), that represent interaction of mGsi and RHO in the absence of the chromophore. (G) Histogram shows the difference between the AUC of samples treated with 9-*cis*-retinal and the AUC of samples treated with DMSO (vehicle). Student's *t*-test for comparison of each adCSNB variant to WT, $*P < 0.05$. (For interpretation of the references to color in this figure legend, the reader is referred to the web version of this article.)

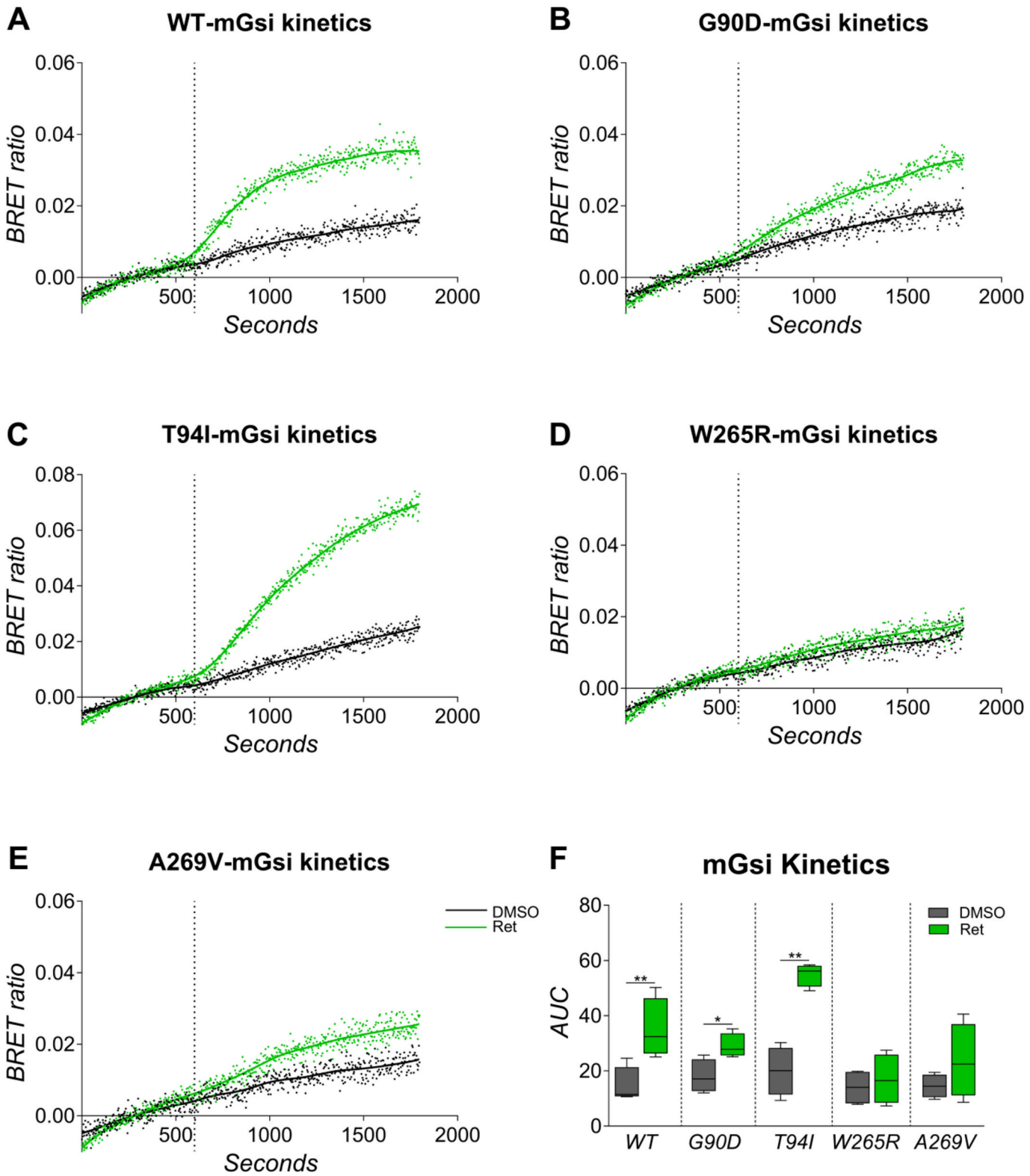

Fig. 6. BRET kinetics of binding of WT RHO and adCSNB pathogenetic variants with mGsi. (A-E) Kinetics curves of binding of WT RHO and adCSNB variants with mGsi in absence of 9-*cis*-retinal (DMSO, black lines) and upon 9-*cis*-retinal treatment (Ret, green lines). The time at which 9-*cis*-retinal was injected is indicated by dotted vertical lines. (F) Box plot represents the Area Under the Curve (AUC) measured in absence (DMSO, grey) or presence (Ret, green) of 9-*cis*-retinal. Student's *t*-test comparing 9-*cis*-retinal treated to untreated; *P < 0.05; **P < 0.01. (For interpretation of the references to color in this figure legend, the reader is referred to the web version of this article.)

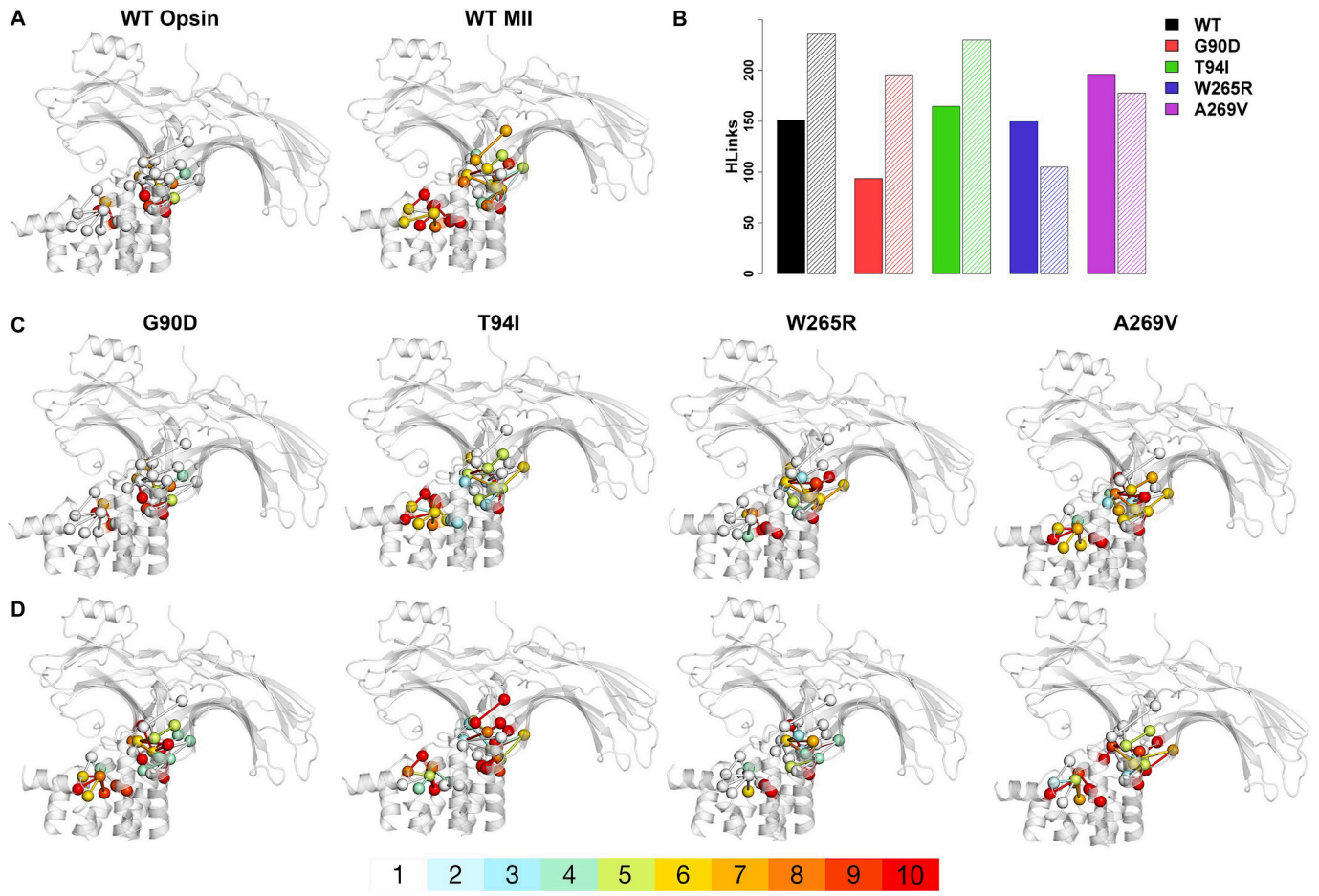

Fig. 7. PSN analysis of the predicted interface in the complexes between the adCSNB variants and ARR1. (A) Cartoon representation of the cryoEM and predicted complexes of WT opsin (PDB: 5w0p) (left) and MII (right) with ARR1 in which the extracellular halves of the receptors are not shown. The native interface-Hlinks are colored according to their interaction strength (see the color legend at the bottom of the figure), whereas nodes are colored according to the average interaction strength of the links they are involved in. (B) The histograms of the summations of the interaction strength of all interfaces native Hlinks for the opsin (filled histograms) and MII (dashed histograms) states are shown for WT (black), G90D (red), T94I (green), W265R (blue), and A269V (violet). (C-D) The predicted complexes between the opsin forms (C) and MII forms (D) of WT and CSNB variants and ARR1 are shown. The native interface-Hlinks and the involved nodes are colored according to the interaction strength. (For interpretation of the references to color in this figure legend, the reader is referred to the web version of this article.)

contributed by the finger loop of ARR1 and H2, H6, H8, and IL1 of RHO, whereas the second hot region involved the strands 5, 6, 9, 15, and 16 and the C-loop of ARR1 and H5 and IL2 of RHO (Figs. 7, S3B and Table S2). Both regions were strengthened in the predicted native complex with MII compared to opsin (Fig. 7). As shown for mGi, the summations of the Hlink forces distinguished the opsin and MII forms of WT RHO, being 151.07 % and 235.57 %, respectively (Fig. 7B and Table S2). The same index computed on the adCSNB variants indicated that, while the strength of the interface for the WT and both H2-variants augmented from opsin to MII, the two H6-variants showed a decreased index (Fig. 7B-D, Table S2).

With the aim of assessing coupling of RHO to ARR1 by BRET assay, we were aware that COS-7 cells do not express the GRK1 enzyme necessary for phosphorylation of the carboxy-terminal region of RHO and for ARR1 recruitment. Furthermore, no rod photoreceptor specific cell line expressing GRK1 was available. To overcome this limitation, we took advantage of a modified ARR1 (tARR1), which lacks of the C-term domain, and that was previously shown to be able to bind to activated RHO in a phosphorylation-independent manner [20,41]. tARR1 linked to YFP was, thus, used for BRET assays. Experimental conditions were optimized upon testing different concentrations of RHO-RLuc8 and increasing amounts of tARR1-YFP (Fig. S9 and 8). Coupling experiments confirmed specific binding of WT RHO to tARR1 which occurred only after exposure to 9-*cis*-retinal, indicating that tARR1 was able to bind only to activated RHO. WT RHO displayed the highest BRET coupling signal to tARR1 and H2-variants recorded a coupling similar to WT RHO (Fig. 8A-C and F). Otherwise, W265R and A269V mutations significantly reduced binding to tARR1, in particular W265R appeared to be unable to bind (Fig. 8D-F). Interestingly, for both opsin and MII states, the BRET AUC values linearly correlated with the values of Hlink interaction strength ($R^2 = 0.92$ and $R^2 = 0.96$, respectively, Fig. S10).

We analyzed 9-*cis*-retinal-dependent coupling kinetics between RHO-Rluc8 and tARR1-YFP (Fig. 9). The coupling curve of WT RHO reached a plateau three-times higher than vehicle-treated controls 400 s after 9-*cis*-retinal injection (Fig. 9A). Differently, all adCSNB mutants failed to attain a plateau and displayed different kinetics with the exception of A269V, that displayed maximal coupling at a time around 1000 s (Fig. 9B-E). The G90D variant had a slower but constantly increasing interaction with tARR1 and, similarly, the coupling curve of the T94I constantly increased over time reaching interaction values higher than WT RHO, but without getting to a plateau (Fig. 9B and C). W265R was the only variants that did not display any binding to tARR1 in the presence or absence of 9-*cis*-retinal (Fig. 9D), as also confirmed by the quantification of the effect of retinal (Fig. 9F).

Altogether these data suggested a slower kinetic of binding of the adCSNB pathogenetic variants to ARR1 with W265R failing the binding

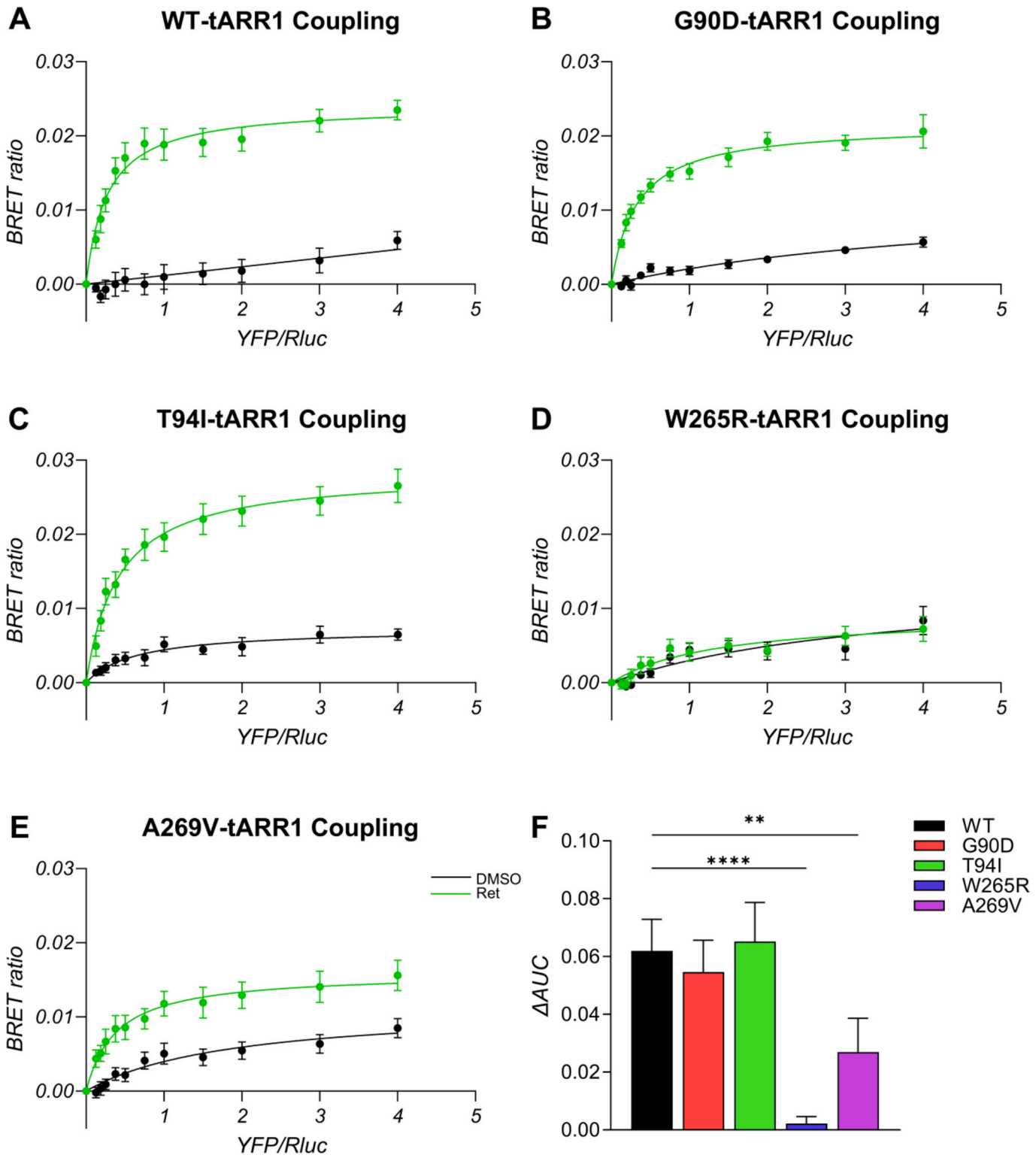

Fig. 8. BRET coupling of WT RHO and adCSNB variants with tARR1. (A-E) Coupling of either RHO WT or adCSNB variants with tARR1 (aa 1–378) was assessed by BRET in the presence (Ret, green lines) or absence (DMSO, black lines) of 9-*cis*-retinal. F Histogram represents the difference of Area Under the Curve (AUC) quantified from the BRET signal of samples treated with 9-*cis*-retinal and of samples treated with DMSO (vehicle). Student's *t*-test, **P < 0.01, ***P < 0.001. (For interpretation of the references to color in this figure legend, the reader is referred to the web version of this article.)

with ARR1 upon activation.

4. Discussion

In this study we report the identification of two new causative pathogenetic variants in *RHO* linked to adCSNB and their molecular characterization *via* a multidisciplinary approach. The H6-variants, W265R and A269V, were compared to two previously reported variants lying in H2, G90D and T94I, already characterized at atomic detail [18,19], with the aim of unraveling common or differential mechanisms

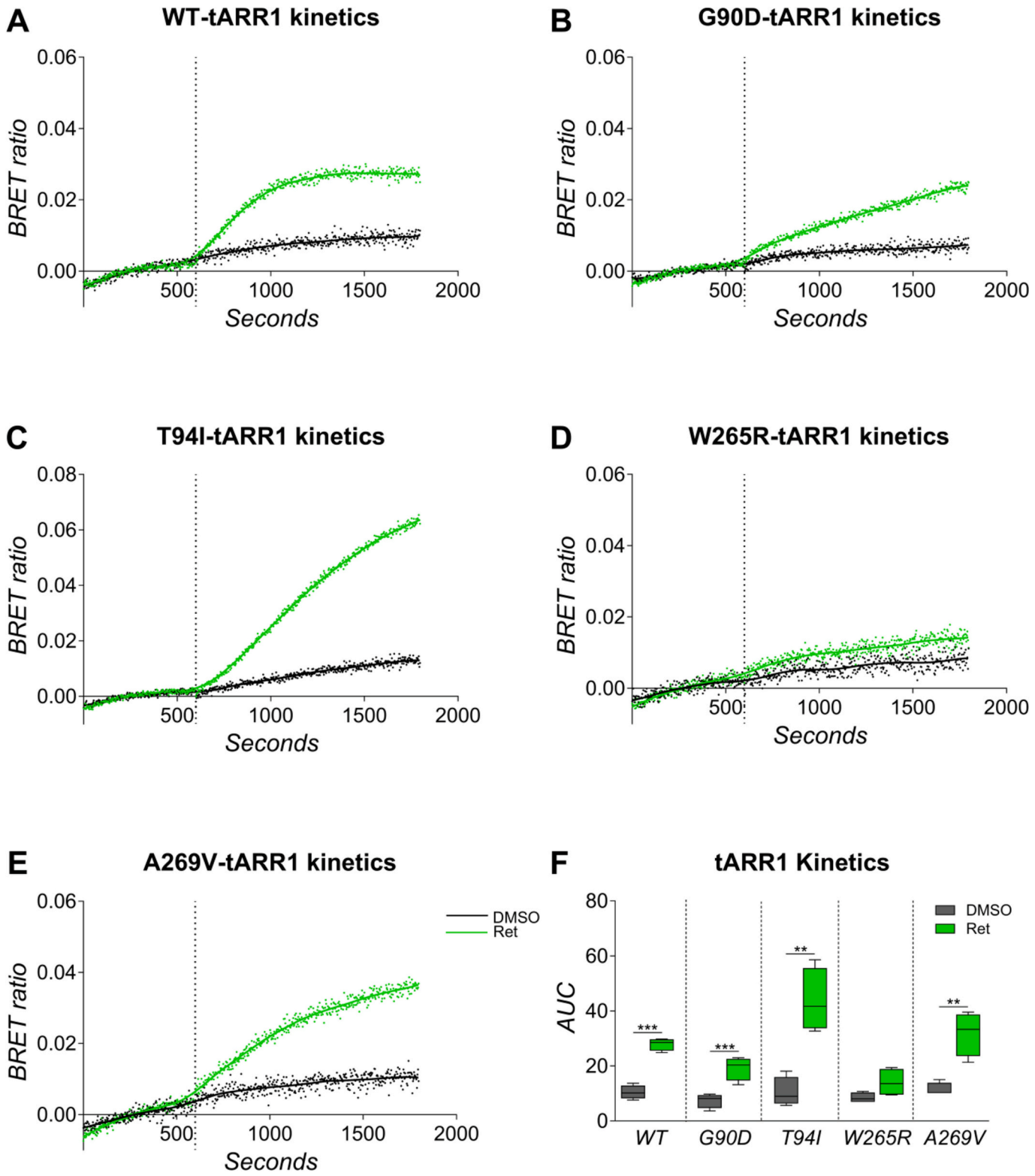

Fig. 9. BRET kinetics of binding of WT RHO and adCSNB pathogenetic variants with tARR1. (A-E) Kinetics curves of binding of either WT RHO or adCSNB RHO variants with tARR1 (aa 1–378) in the absence of 9-*cis*-retinal (DMSO, black lines) and upon 9-*cis*-retinal treatment (Ret, green lines). The time at which 9-*cis*-retinal was injected is indicated by dotted vertical lines. (F) Box plot represents Area Under the Curve (AUC) measured in absence (DMSO, grey) or presence (Ret, green) of 9-*cis*-retinal. Student's t-test comparing 9-*cis*-retinal treated to untreated; *P < 0.05; **P < 0.01. (For interpretation of the references to color in this figure legend, the reader is referred to the web version of this article.)

leading to the adCSNB phenotype. We report no major misfolding caused by adCSNB mutations based on *in silico* and *in vitro* studies, and these data confirmed previously published studies on G90D and T94I [42]. The W265R variant increased retention in the ER upon binding with 11-*cis*-retinal, differently from RHO variants causing RP. We could explain this behavior by *in silico* analysis showing that the arginine substitution for W265 perturbs the native interaction network in the retinal binding site.

Molecular simulations showed that, by different intrinsic dynamics, the H6-variants affect the motions of IL2 and the cytosolic extensions of H5 and H6, and H8, thus deforming the binding sites to G protein and ARR1, which in part overlap each other. Notably, docking simulation suggested that folding of IL2 in a two-turn α-helix is important for the establishment of a strong native-like interface between opsin and ARR1. On these bases, the impaired coupling of RHO mutants with ARR1 might be ascribed, at least in part, to failure for IL2 to acquire the peculiar conformation. The structural effects of mutations on the hot regions at the interfaces between RHO and either mGi or ARR1, identified H6-variants as causing constitutive coupling with mGi, which appeared stronger than in WT RHO. For WT and H2-variants, in particular T94I, the presence of retinal improved the interface hot region, while a worsening was observed for the two H6-variants, in particular W265R. Indeed, the W265 residue is highly conserved in Family A GPCRs and mediates the structural communication between ligand binding site of the receptor and G protein/arrestin coupling regions in the vast majority of structural complexes solved so far [43].

Differently from H6-variants, H2-variants showed low or no constitutive coupling with mGsi and T94I could be light-stimulated to even higher levels than WT and G90D. Nevertheless, H2-variants had slow binding kinetics that could not reach a plateau in the time of the BRET experiments. The low response to retinal of G90D may be explained, at least in part, by some constitutive coupling of the RHO variant to the G protein, as detected in the kinetics experiments (see Fig. 6B black curve). Our results are, thus, consistent with previous studies showing that G90D is in an active configuration and that remains activated for longer time [42,44]. Our data also agree with the most recent report uncovering that G90D produces, irrespective of retinal, continuous noise in darkness due to concatenated electrical events of low amplitude and high frequency [45]. The BRET assay, otherwise, identified T94I as a mutant that binds to mGsi at higher levels that WT RHO, but with slower kinetics. The finding of increased interaction with G protein also confirms the prolonged MII state for this mutant. In fact, the BRET results do not diverge from a biochemical study on the constitutive activation of both G90D and T94I, that identified G90D as more capable to activate Gt [14,15], because the kinetics of G90D coupling to mGsi in the absence of 9-*cis*-retinal, was faster than the kinetics of T94I. The BRET coupling studies on H2-variants with tARR1 are also in agreement with the literature that reports a reduced binding to ARR1 for G90D but not for T94I [20].

A common feature of adCSNB mutations in RHO is that they affect interactions with K296 in the retinal pocket [2]. Nevertheless, while the four variants are linked to a CSNB phenotype, our results show that the allosteric structural changes in the cytosolic regions caused by variants in H2 or H6 are different and may differently affect RHO functionality. Coupling and kinetics studies suggested that, while the different adCSNB RHO pathogenetic variants are characterized by prolonged activation of RHO, the alteration caused by variants lying in H6 are distinctive from those lying in H2. RHO W265R and A269V variants showed no or very limited changes in binding to G protein when reconstituted with 9-*cis*-retinal, possibly because the two amino acid substitutions in H6 cause a conformational change that allows RHO to interact with the G protein without the need of retinal isomerization. Moreover, the phenotype for these two RHO variants might also be amplified by the altered or low binding with ARR1. This effect was mainly evident for the RHO W265R variant, which failed to bind to tARR1. The constitutive activity of the two H6-variants towards mGi coupling, combined with reduced desensitization by ARR1, could synergistically contribute to maintain active phototransduction, that characterizes the adCSNB phenotype. Differently, most mutations linked to RP cause misfolding and ER retention, and, when localized at the retinal binding pocket, they perturb the pocket volume [12]. This study provides a molecular explanation of the different phenotypes in RP and CSNB patients.

5. Conclusion

In the present study, the combination of molecular modeling and simulations with subcellular localization analysis and BRET coupling led us to gain insights into the structural characteristics of two novel RHO mutants in helix 6. Specifically, W265 and A269 locate two positions upstream and downstream of the highly conserved P267 residue, which confers functionally important conformational degrees of freedom to helix 6. Arginine substitution for W265 induces the formation of a salt bridge with E122 on H3, whereas valine substitution for A296 alters local H5-H6 packing interactions. Such local perturbations in the mutation site, while not causing misfolding, affect the structural communication between retinal binding site and G protein/arrestin binding regions of the RHO protein. Based on this evidence, we propose that the H6-variants share light-independent coupling with the G protein with a conformation similar to the activated RHO. The constitutive activation of the G protein is exacerbated by reduced desensitization due to impaired binding to ARR1 upon light-stimulation. On the contrary, mutations on H2 alter the kinetics of activation and deactivation of RHO, leading to slower recycling of the receptor and, hence, causing night blindness.

CRediT authorship contribution statement

Andrea Bighinati: Writing – original draft, Formal analysis, Data curation, Investigation, Methodology, Validation, Visualization, Writing – review & editing. **Sara D'Alessandro:** Writing – original draft, Formal analysis, Data curation, Investigation, Methodology, Validation, Visualization, Writing – review & editing. **Angelo Felline:** Formal analysis, Investigation, Methodology, Software, Visualization, Writing – review & editing. **Christina Zeitz:** Formal analysis, Investigation, Validation. **Béatrice Bocquet:** Formal analysis, Investigation, Validation. **Livio Casarini:** Supervision, Methodology. **Vasiliki Kalatzis:** Writing – review & editing. **Isabelle Meunier:** Investigation. **Francesca Fanelli:** Writing – review & editing, Funding acquisition, Formal analysis, Conceptualization, Investigation, Methodology, Resources, Visualization. **Gaël Manes:** Writing – review & editing, Funding acquisition, Conceptualization, Investigation, Methodology, Visualization. **Valeria Marigo:** Writing – review & editing, Funding acquisition, Conceptualization, Project administration, Resources, Supervision, Writing – original draft.

Declaration of competing interest

Authors A.B., S.DA., A.F., C.Z., B.B., F.F., L.C., V.K., I.M. and G.M. declare they have no competing financial interests. Author V.M. is shareholder of the company Mireca Medicines.

Data availability

Data will be made available on request.

Acknowledgments

We sincerely thank members of the families involved in this study. The authors acknowledge the Cell-lab facility of University of Modena and Reggio Emilia for providing cell culture assistance.

Funding sources

This work was supported by grants from EJP RD 2020 (EJPRD20-101 TreatRP) to V.M., Unione europea – Next Generation EU PRIN 2022 - Piano Nazionale di Ripresa e Resilienza a titolarità del Ministero dell'Università e della Ricerca (2022R9BKZN) and Fondazione Telethon (GGP19113) to V.M.; PIANO NAZIONALE DI RIPRESA E RESILIENZA (PNRR) — MISSIONE 4 "Istruzione Ricerca" COMPONENTE 2, "Dalla ricerca all'impresa" INVESTIMENTO 1.4, "Potenziamento strutture di ricerca e creazione di "campioni nazionali di R&S" su alcune Key enabling technologies", finanziato dall'Unione europea – NextGenerationEU "National Center for Gene Therapy and Drugs based on RNA Technology" cod. Progetto CN00000041 (2022–2025) and PIANO NAZIONALE DI RIPRESA E RESILIENZA (PNRR) — MISSIONE 4 "Istruzione Ricerca" COMPONENTE 2, "Dalla ricerca all'impresa" INVESTIMENTO 1.4, "Potenziamento strutture di ricerca e creazione di "campioni nazionali di R&S" su alcune Key enabling technologies", finanziato dall'Unione europea – NextGenerationEU Paternariato Esteso HEAL ITALIA (2022–2025), to V.M. and F.F.; SOS Rétinite Pigmentaire foundation (#20142016/1051 Montpellier, France) and Programme Hospitalier de Recherche Clinique (PHRC; #12-014-0041) (Paris, France) for a fellowship to G.M.

Appendix A. Supplementary data

Supplementary data to this article can be found online at https://doi.org/10.1016/j.ijbiomac.2024.135089.

References

[1] C. Zeitz, A.G. Robson, I. Audo, Congenital stationary night blindness: an analysis and update of genotype-phenotype correlations and pathogenic mechanisms, Prog. Retin. Eye Res. 45 (2015) 58–110, https://doi.org/10.1016/j.preteyeres.2014.09.001.

[2] S.D. McAlear, T.W. Kraft, A.K. Gross, 1 rhodopsin mutations in congenital night blindness, in: Adv Exp Med Biol, 2010, pp. 263–272, https://doi.org/10.1007/978-1-4419-1399-9_30.

[3] I. Audo, G. Manes, S. Mohand-Saïd, A. Friedrich, M.-E. Lancelot, A. Antonio, V. Moskova-Doumanova, O. Poch, X. Zanlonghi, C.P. Hamel, J.-A. Sahel, S. S. Bhattacharya, C. Zeitz, Spectrum of rhodopsin mutations in French autosomal dominant rod-cone dystrophy patients, Invest. Ophthalmol. Vis. Sci. 51 (2010) 3687–3700, https://doi.org/10.1167/iovs.09-4766.

[4] A. Kartasasmita, K. Fujiki, E. Iskandar, I. Sovani, T. Fujimaki, A. Murakami, A novel nonsense mutation in rhodopsin gene in two Indonesian families with autosomal recessive retinitis pigmentosa, Ophthalmic Genet. 32 (2011) 57–63, https://doi.org/10.3109/13816810.2010.535892.

[5] G. Kumaramanickavel, M. Maw, M.J. Denton, S. John, C.R. Srikumari, U. Orth, R. Oehlmann, A. Gal, Missense rhodopsin mutation in a family with recessive RP, Nat. Genet. 8 (1994) 10–11, https://doi.org/10.1038/ng0994-10.

[6] K. Palczewski, G protein-coupled receptor rhodopsin, Annu. Rev. Biochem. 75 (2006) 743–767, https://doi.org/10.1146/annurev.biochem.75.103004.142743.

[7] K.P. Hofmann, P. Scheerer, P.W. Hildebrand, H.-W. Choe, J.H. Park, M. Heck, O. P. Ernst, A G protein-coupled receptor at work: the rhodopsin model, Trends Biochem. Sci. 34 (2009) 540–552, https://doi.org/10.1016/j.tibs.2009.07.005.

[8] N. al-Jandal, G.J. Farrar, A.S. Kiang, M.M. Humphries, N. Bannon, J.B. Findlay, P. Humphries, P.F. Kenna, A novel mutation within the rhodopsin gene (Thr-94-Ile) causing autosomal dominant congenital stationary night blindness, Hum. Mutat. 13 (1999) 75–81, https://doi.org/10.1002/(SICI)1098-1004(1999)13:1<75::AID-HUMU9>3.0.CO;2-4.

[9] T.P. Dryja, E.L. Berson, V.R. Rao, D.D. Oprian, Heterozygous missense mutation in the rhodopsin gene as a cause of congenital stationary night blindness, Nat. Genet. 4 (1993) 280–283, https://doi.org/10.1038/ng0793-280.

[10] C. Reiff, M. Owczarek-Lipska, G. Spital, C. Röger, H. Hinz, C. Jüschke, H. Thiele, J. Altmüller, P. Nürnberg, R. Da Costa, J. Neidhardt, The mutation p.E113K in the Schiff base counterion of rhodopsin is associated with two distinct retinal phenotypes within the same family, Sci. Rep. 6 (2016) 36208, https://doi.org/10.1038/srep36208.

[11] V.R. Rao, G.B. Cohen, D.D. Oprian, Rhodopsin mutation G90D and a molecular mechanism for congenital night blindness, Nature 367 (1994) 639–642, https://doi.org/10.1038/367639a0.

[12] P. Behnen, A. Felline, A. Comitato, M.T. Di Salvo, F. Raimondi, S. Gulati, S. Kahremany, K. Palczewski, V. Marigo, F. Fanelli, A small chaperone improves folding and routing of rhodopsin mutants linked to inherited blindness, IScience 4 (2018) 1–19, https://doi.org/10.1016/j.isci.2018.05.001.

[13] D. Athanasiou, M. Aguila, J. Bellingham, W. Li, C. McCulley, P.J. Reeves, M. E. Cheetham, The molecular and cellular basis of rhodopsin retinitis pigmentosa reveals potential strategies for therapy, Prog. Retin. Eye Res. 62 (2018) 1–23, https://doi.org/10.1016/j.preteyeres.2017.10.002.

[14] A.K. Gross, G. Xie, D.D. Oprian, Slow binding of retinal to rhodopsin mutants G90D and T94D, Biochemistry 42 (2003) 2002–2008, https://doi.org/10.1021/bi020612r.

[15] A.K. Gross, V.R. Rao, D.D. Oprian, Characterization of rhodopsin congenital night blindness mutant T94I, Biochemistry 42 (2003) 2009–2015, https://doi.org/10.1021/bi020613j.

[16] C. Zeitz, A.K. Gross, D. Leifert, B. Kloeckener-Gruissem, S.D. McAlear, J. Lemke, J. Neidhardt, W. Berger, Identification and functional characterization of a novel rhodopsin mutation associated with autosomal dominant CSNB, Invest. Opthalmol. Vis. Sci. 49 (2008) 4105, https://doi.org/10.1167/iovs.08-1717.

[17] A.M. Dizhoor, M.L. Woodruff, E.V. Olshevskaya, M.C. Cilluffo, M.C. Cornwall, P. A. Sieving, G.L. Fain, Night blindness and the mechanism of constitutive signaling of mutant G90D rhodopsin, J. Neurosci. 28 (2008) 11662–11672, https://doi.org/10.1523/JNEUROSCI.4006-08.2008.

[18] A. Singhal, M.K. Ostermaier, S.A. Vishnivetskiy, V. Panneels, K.T. Homan, J.J. G. Tesmer, D. Veprintsev, X. Deupi, V.V. Gurevich, G.F.X. Schertler, J. Standfuss, Insights into congenital stationary night blindness based on the structure of G90D rhodopsin, EMBO Rep. (2013), https://doi.org/10.1038/embor.2013.44.

[19] A. Singhal, Y. Guo, M. Matkovic, G. Schertler, X. Deupi, E.C. Yan, J. Standfuss, M. Smit, H. Vischer, R. Bakker, A. Jongejan, H. Timmerman, L. Pardo, R. Leurs, D. Baylor, B. Nunn, J. Schnapf, T. Melia, C. Cowan, J. Angleson, T. Wensel, P. Park, P. Robinson, G. Cohen, E. Zhukovsky, D. Oprian, J. Rim, D. Oprian, V. Rao, G. Cohen, D. Oprian, A. Gross, V. Rao, D. Oprian, P. Sieving, J. Richards, F. Naarendorp, E. Bingham, K. Scott, M. Alpern, C. Zeitz, A. Gross, D. Leifert, B. Kloeckener-Gruissem, S. McAlear, J. Lemke, J. Neidhardt, W. Berger, N. Al-Jandal, G. Farrar, A. Kiang, M. Humphries, N. Bannon, J. Findlay, P. Humphries, P. Kenna, S. McAlear, T. Kraft, A. Gross, P. Sieving, M. Fowler, R. Bush, S. Machida, P. Calvert, D. Green, C. Makino, C. McHenry, A. Dizhoor, M. Woodruff, E. Olshevskaya, M. Cilluffo, M. Cornwall, P. Sieving, G. Fain, M. Naash, T. Wu, D. Chakraborty, S. Fliesler, X. Ding, M. Nour, N. Peachey, J. Lem, N. Qtaishat, M. Al-Ubaidi, A. Singhal, M. Ostermaier, S. Vishnivetskiy, V. Panneels, K. Homan, J. Tesmer, D. Veprintsev, X. Deupi, V. Gurevich, G. Schertler, H. Choe, Y. Kim, J. Park, T. Morizumi, E. Pai, N. Krauss, K. Hofmann, P. Scheerer, O. Ernst, G. Xie, A. Gross, D. Oprian, J. Standfuss, G. Xie, P. Edwards, M. Burghammer, D. Oprian, G. Schertler, J. Standfuss, E. Zaitseva, M. Mahalingam, R. Vogel, X. Deupi, P. Edwards, A. Singhal, B. Nickle, D. Oprian, G. Schertler, J. Standfuss, A. Cooper, S. Dixon, M. Nutley, Y. Guo, S. Sekharan, J. Liu, V. Batista, J. Tully, E. Yan, J. Janz, D. Farrens, J. Liu, M. Liu, J. Nguyen, A. Bhagat, V. Mooney, E. Yan, R. Piechnick, E. Ritter, P. Hildebrand, O. Ernst, P. Scheerer, K. Hofmann, M. Heck, J. Liu, M. Liu, L. Fu, G. Zhu, E. Yan, J. Liu, M. Liu, J. Nguyen, A. Bhagat, V. Mooney, E. Yan, D. Toledo, E. Ramon, M. Aguilà, A. Cordomí, J. Pérez, H. Mendes, M. Cheetham, P. Garriga, J. Kim, C. Altenbach, M. Kono, D. Oprian, W. Hubbell, H. Khorana, S. Kawamura, A. Colozo, L. Ge, D. Muller, P. Park, E. Zhukovsky, D. Oprian, T. Sakmar, R. Franke, H. Khorana, K. Fahmy, T. Zvyaga, T. Sakmar, F. Siebert, E. Ramon, L. del Valle, P. Garriga, T. Zvyaga, K. Fahmy, F. Siebert, T. Sakmar, R. Vogel, F. Siebert, S. Vishnivetskiy, M. Ostermaier, A. Singhal, V. Panneels, K. Homan, A. Glukhova, S. Sligar, J. Tesmer, G. Schertler, J. Standfuss, S. Jin, M. Cornwall, D. Oprian, M. Mahalingam, K. Martínez-Mayorga, M. Brown, R. Vogel, D. Mattle, A. Singhal, G. Schmid, R. Dawson, J. Standfuss, W. Kabsch, A. McCoy, R. Grosse-Kunstleve, P. Adams, M. Winn, L. Storoni, R. Read, P. Emsley, K. Cowtan, P. Adams, R. Grosse-Kunstleve, L. Hung, T. Ioerger, A. McCoy, N. Moriarty, R. Read, J. Sacchettini, N. Sauter, T. Terwilliger, A. Alexandrov, M. Mileni, E. Chien, M. Hanson, R. Stevens, M. Liu, J. Liu, D. Mehrotra, Y. Liu, Y. Guo, P. Baldera-Aguayo, V. Mooney, A. Nour, E. Yan, J. Li, P. Edwards, M. Burghammer, C. Villa, G. Schertler, J. Phillips, R. Braun, W. Wang, J. Gumbart, E. Tajkhorshid, E. Villa, C. Chipot, R. Skeel, L. Kalé, K. Schulten, A. MacKerell, D. Bashford, M. Bellott, Structural role of the T94I rhodopsin mutation in congenital stationary night blindness, EMBO Rep. 47 (2016) e201642671, https://doi.org/10.15252/embr.201642671.

[20] S.A. Vishnivetskiy, M.K. Ostermaier, A. Singhal, V. Panneels, K.T. Homan, A. Glukhova, S.G. Sligar, J.J.G. Tesmer, G.F.X. Schertler, J. Standfuss, V. V. Gurevich, Constitutively active rhodopsin mutants causing night blindness are effectively phosphorylated by GRKs but differ in arrestin-1 binding, Cell. Signal. 25 (2013) 2155–2162, https://doi.org/10.1016/j.cellsig.2013.07.009.

[21] M.F. Marmor, A.B. Fulton, G.E. Holder, Y. Miyake, M. Brigell, M. Bach, International Society for Clinical Electrophysiology of Vision, ISCEV Standard for full-field clinical electroretinography (2008 update), Doc. Ophthalmol. 118 (2009) 69–77, https://doi.org/10.1007/s10633-008-9155-4.

[22] A. Felline, D. Schiroli, A. Comitato, V. Marigo, F. Fanelli, Structure network-based landscape of rhodopsin misfolding by mutations and algorithmic prediction of small chaperone action, Comput. Struct. Biotechnol. J. 19 (2021) 6020–6038, https://doi.org/10.1016/j.csbj.2021.10.040.

[23] B.R. Brooks, C.L. Brooks, A.D. Mackerell, L. Nilsson, R.J. Petrella, B. Roux, Y. Won, G. Archontis, C. Bartels, S. Boresch, A. Caflisch, L. Caves, Q. Cui, A.R. Dinner, M. Feig, S. Fischer, J. Gao, M. Hodoscek, W. Im, K. Kuczera, T. Lazaridis, J. Ma, V. Ovchinnikov, E. Paci, R.W. Pastor, C.B. Post, J.Z. Pu, M. Schaefer, B. Tidor, R. M. Venable, H.L. Woodcock, X. Wu, W. Yang, D.M. York, M. Karplus, CHARMM: the biomolecular simulation program, J. Comput. Chem. 30 (2009) 1545–1614, https://doi.org/10.1002/jcc.21287.

[24] W. Im, M. Feig, C.L. Brooks, An implicit membrane generalized born theory for the study of structure, stability, and interactions of membrane proteins, Biophys. J. 85 (2003) 2900–2918, https://doi.org/10.1016/S0006-3495(03)74712-2.

[25] J.H. Park, P. Scheerer, K.P. Hofmann, H.-W. Choe, O.P. Ernst, Crystal structure of the ligand-free G-protein-coupled receptor opsin, Nature 454 (2008) 183–187, https://doi.org/10.1038/nature07063.
[26] P. Scheerer, J.H. Park, P.W. Hildebrand, Y.J. Kim, N. Krauß, H.-W. Choe, K. P. Hofmann, O.P. Ernst, Crystal structure of opsin in its G-protein-interacting conformation, Nature 455 (2008) 497–502, https://doi.org/10.1038/nature07330.
[27] A. Felline, S. Conti, M. Seeber, M. Cecchini, F. Fanelli, Wordom update 2: a user-friendly program for the analysis of molecular structures and conformational ensembles, Comput. Struct. Biotechnol. J. 21 (2023) 1390–1402, https://doi.org/10.1016/j.csbj.2023.01.026.
[28] M. Seeber, A. Felline, F. Raimondi, S. Muff, R. Friedman, F. Rao, A. Caflisch, F. Fanelli, Wordom: a user-friendly program for the analysis of molecular structures, trajectories, and free energy surfaces, J. Comput. Chem. 32 (2011) 1183–1194, https://doi.org/10.1002/jcc.21688.
[29] B.G. Pierce, Y. Hourai, Z. Weng, Accelerating protein docking in ZDOCK using an advanced 3D convolution library, PLoS One 6 (2011) e24657, https://doi.org/10.1371/journal.pone.0024657.
[30] D. Casciari, M. Seeber, F. Fanelli, Quaternary structure predictions of transmembrane proteins starting from the monomer: a docking-based approach, BMC Bioinformatics 7 (2006) 340, https://doi.org/10.1186/1471-2105-7-340.
[31] Y. Kang, O. Kuybeda, P.W. de Waal, S. Mukherjee, N. Van Eps, P. Dutka, X.E. Zhou, A. Bartesaghi, S. Erramilli, T. Morizumi, X. Gu, Y. Yin, P. Liu, Y. Jiang, X. Meng, G. Zhao, K. Melcher, O.P. Ernst, A.A. Kossiakoff, S. Subramaniam, H.E. Xu, Cryo-EM structure of human rhodopsin bound to an inhibitory G protein, Nature 558 (2018) 553–558, https://doi.org/10.1038/s41586-018-0215-y.
[32] X.E. Zhou, Y. He, P.W. de Waal, X. Gao, Y. Kang, N. Van Eps, Y. Yin, K. Pal, D. Goswami, T.A. White, A. Barty, N.R. Latorraca, H.N. Chapman, W.L. Hubbell, R. O. Dror, R.C. Stevens, V. Cherezov, V.V. Gurevich, P.R. Griffin, O.P. Ernst, K. Melcher, H.E. Xu, Identification of phosphorylation codes for arrestin recruitment by G protein-coupled receptors, Cell 170 (2017) 457–469.e13, https://doi.org/10.1016/j.cell.2017.07.002.
[33] C.-J. Tsai, J. Marino, R. Adaixo, F. Pamula, J. Muehle, S. Maeda, T. Flock, N. M. Taylor, I. Mohammed, H. Matile, R.J. Dawson, X. Deupi, H. Stahlberg, G. Schertler, Cryo-EM structure of the rhodopsin-Gαi-βγ complex reveals binding of the rhodopsin C-terminal tail to the gβ subunit, Elife 8 (2019) e46041, https://doi.org/10.7554/eLife.46041.
[34] A. Felline, M. Seeber, F. Fanelli, PSNtools for standalone and web-based structure network analyses of conformational ensembles, Comput. Struct. Biotechnol. J. 20 (2022) 640–649, https://doi.org/10.1016/j.csbj.2021.12.044.
[35] Q. Wan, N. Okashah, A. Inoue, R. Nehmé, B. Carpenter, C.G. Tate, N.A. Lambert, Mini G protein probes for active G protein-coupled receptors (GPCRs) in live cells, J. Biol. Chem. 293 (2018) 7466–7473, https://doi.org/10.1074/jbc.RA118.001975.
[36] C.-J. Tsai, F. Pamula, R. Nehmé, J. Mühle, T. Weinert, T. Flock, P. Nogly, P. C. Edwards, B. Carpenter, T. Gruhl, P. Ma, X. Deupi, J. Standfuss, C.G. Tate, G.F. X. Schertler, Crystal structure of rhodopsin in complex with a mini-G $_o$ sheds light on the principles of G protein selectivity, Sci. Adv. 4 (2018), https://doi.org/10.1126/sciadv.aat7052.
[37] F. Fanelli, P.G. De Benedetti, Update 1 of: computational modeling approaches to structure–function analysis of G protein-coupled receptors, Chem. Rev. 111 (2011) PR438–PR535, https://doi.org/10.1021/cr100437t.
[38] Y. Gao, H. Hu, S. Ramachandran, J.W. Erickson, R.A. Cerione, G. Skiniotis, Structures of the rhodopsin-transducin complex: insights into G-protein activation, Mol. Cell 75 (2019) 781–790.e3, https://doi.org/10.1016/j.molcel.2019.06.007.
[39] O. Keskin, A. Gursoy, B. Ma, R. Nussinov, Principles of protein-protein interactions: what are the preferred ways for proteins to interact? Chem. Rev. 108 (2008) 1225–1244, https://doi.org/10.1021/cr040409x.
[40] M.I. Simon, M.P. Strathmann, N. Gautam, Diversity of G proteins in signal transduction, Science 252 (1991) 802–808, https://doi.org/10.1126/science.1902986.
[41] K. Palczewski, J. Buczylko, H. Ohguro, R.S. Annan, S.A. Carr, J.W. Crabb, M. W. Kaplan, R.S. Johnson, K.A. Walsh, Characterization of a truncated form of arrestin isolated from bovine rod outer segments, Protein Sci. 3 (1994) 314–324, https://doi.org/10.1002/pro.5560030215.
[42] P.S.-H. Park, Constitutively active rhodopsin and retinal disease, Adv. Pharmacol. 70 (2014) 1–36, https://doi.org/10.1016/B978-0-12-417197-8.00001-8.
[43] A. Felline, S. Gentile, F. Fanelli, psnGPCRdb: the structure-network database of G protein coupled receptors, J. Mol. Biol. 435 (2023) 167950, https://doi.org/10.1016/J.JMB.2023.167950.
[44] K.S. Shindler, E. Ventura, T.S. Rex, P. Elliott, A. Rostami, SIRT1 activation confers neuroprotection in experimental optic neuritis, Invest. Ophthalmol. Vis. Sci. 48 (2007) 3602–3609, https://doi.org/10.1167/iovs.07-0131.
[45] Z. Chai, Y. Ye, D. Silverman, K. Rose, A. Madura, R.R. Reed, J. Chen, K.-W. Yau, Dark continuous noise from mutant G90D-rhodopsin predominantly underlies congenital stationary night blindness, Proc. Natl. Acad. Sci. USA 121 (2024) e2404763121, https://doi.org/10.1073/pnas.2404763121.